Experimental testing of wind turbine rotors for enhanced wake diffusion

Viljar Dyvik Sellevold

Bachelor's thesis in Energy Technology
Bergen, Norway 2024

Høgskulen på Vestlandet

Experimental testing of wind turbine rotors for enhanced wake diffusion

Viljar Dyvik Sellevold

Department of Mechanical Engineering and Maritime Studies
Western Norway University of Applied Sciences
NO-5063 Bergen, Norge

Høgskulen på Vestlandet
Department of Mechanical Engineering and Maritime Studies
Inndalsveien 28,
NO-5063 Bergen, Norge

Norsk tittel:	Eksperimentell testing av vindturbinrotor for redusert vakeeffekt
Author(s), student number:	Viljar Dyvik Sellevold, 596222
Study program:	Energy Technology
Date:	May 2024
Report number:	IMM 2024-M 84
Supervisor at HVL:	Jan Michael Simon Bartl
Assigned by:	HVL
Contact person:	Jan Michael Simon Bartl
Antall filer levert digitalt:	1

Preface

This bachelor's thesis is written at the Department of Mechanical and Marine Engineering for the Western University of Applied Science (HVL) as part of the bachelor's program in Energy Technology. The thesis is written in collaboration with HVL as part of an on-going study in the MarinLab and is supervised by Associate Professor Jan Michael Simon Bartl.

First and foremost, I would like to express my gratitude to Associate Professor Jan Michael Simon Bartl, not only for introducing me to the wake-diffusion rotor concept and wind energy in general, but also for passionately sharing his knowledge and providing excellent guidance throughout the project.

The work investigated in this thesis has been a close and productive collaboration between myself and master student Felix Raupach, which is writing his own master thesis on the same project. The underlying areas of responsibility is listed below.

	Felix	Viljar
Designing rotor blade and new parts (Autodesk Fusion 360)		x
Aerodynamic design (QBlade)	x	
3D printing	x	x
Conducting experiments	x	x
Performance measurements		x
Post-processing - Performance data (Matlab)		x
LPTV-measurements	x	
Post-processing - LPTV data (DaVis10)	x	

I would like to thank Felix Raupach for the time working together on this project and for being a reliable partner with a keen eye for detail.

Thanks to all the lab engineers at HVL, Kjetil Gravelsæter, Frode Wessel Jansen, Nafez Ardestani, Harald Moen and Torstein Frantzen for always being service-minded and gladly sharing their wisdom and expertise.

Abstract

Increasing the energy efficiency of renewable energy resources is a crucial step towards reaching net zero carbon emissions. Optimizing the annual power production (APP) within a wind farm is a topic of current field of research in pursuit of making wind energy more efficient. In this quest, lab scale experiments can provide valuable insight for the potential of increasing a wind farms power output. The wake-diffusion rotor is a concept that potentially can increase the APP of a wind farm, and further investigation of this concept is the underlying motivation for this thesis.

In this work, the wake-diffusion rotor concept is investigated by conducting experiments at MarinLab at Western Norway University of Applied Science (HVL). Rotor blades with an intentionally modified twist angle distributions at the inner part of the blades are being designed and manufactured. Performance data of the resulting rotor sets are being measured, and the three-dimensional flow fields of the wakes at three different positions in the wake, i.e. x/D=2, x/D6 and x/D=10, are captured and analyzed using a Lagrangian Particle Tracking Velocimetry (LPTV).

The outcome of this thesis indicates that the wake-diffusion rotor concept shows promising results when investigating the near wake produced by the different rotor designs at distance x/D=2. The modified blade geometries show higher mean velocities in the center of the wake, initiating in a faster wake diffusion. For larger downstream distances, initial results show a similar kinetic energy content at x/D=6 and x/D=10 in the wake, while a more thorough evaluation is yet to be done for reliable results.

The results indicate a promising potential for increasing the power in wind farm setup, while more detailed studies are needed to draw solid conclusions.

Samandrag

Energieffektivisering av fornybare energiressursar er heilt avgjerande for å nå målet om ein karbonnøytral kraftproduksjon. Å optimalisere den årlege kraftproduksjonen (APP) i ein vindpark for å utnytte vindenergien endå betre er eit forskningsområde med høg aktuelitet. I denne jakta kan små-skala eksperiment utført i kontrollerte omgjevnadar i laboratorie gje god innsikt i korleis virkningsgrada til vindturbinparkar kan bli endå betre. Rotorar designa for reduserte vakeeffektar er eit konsept som foreslår ein måte å oppnå ei betre virkningsgrad i vindturbinparkar på, og undersøkingar knytt til dette konseptet er i så måte motivasjon bak denne oppgåva.

I denne oppgåva er rotordesign for redusert vakeeffekt undersøkt ved å utføre eksperiment i MarinLab ved Høgskulen på Vestlandet (HVL). Rotorblad med tilsikta varierande vridningsvinkeldistribusjon på den innerste delen av rotorbladet er designa og produsert. Prestasjonsdata frå rotorane er målt ved tre ulike distansar, henholdsvis x/D=2, x/D=6 og x/D=10, i tillegg til at vaka si tre-dimensjonale utstrekking er fanga og analysert ved hjelp av eit Lagrangian Particle Tracking Velocimetry-system (LPTV).

Denne oppgåva indikerer at rotorar designa for redusert vakeeffekt syner lovande resultat når den nærliggjande vaka frå dei ulike rotordesigna, ved ein avstand x/D=2, er analysert. Det viser seg at høgre gjennomsnittshastigheiter er observert i midten av vaka frå dei modifiserte bladgeometriane. Dette fører til reduserte vakeeffektar. For distansar lengre nedstrøms, viser dei foreløpige resultata at liknande kinetisk energiinnhald er observert i vaka ved x/D=6 og x/D=10. Grundigare evalueringar er likevel naudsynt for å oppnå pålitelege resultat.

Resultata i denne oppgåva viser at rotorblad designa for reduserte vakeeffektar er eit lovande konsept for å betre virkningsgrada i vindparkar, sjølv om ytterlegare studiar må gjennomførast for å trekke ein konklusjon.

Contents

Nomenclature

Latin characters

Symbol	Meaning	Unit
A	Section area	m^2
A_{swept}	Circular area	m^2
C_D	Drag coefficient	[-]
C_L	Lift coefficient	[-]
C_n	Normal force coefficient	[-]
C_P	Power coefficient	[-]
C_T	Thrust coefficient	[-]
C_t	Tangential force coefficient	[-]
D	Diameter	m
F_L	Lift force	N
F_D	Drag force	N
GW	Giga watt (10^9)	W
l	Length of body	m
N	Newton	N
Nm	Newton meter	Nm
$P_{turbine}$	Power generated by the turbine	W
P_{wind}	Power in the wind	W
R	Radius of the turbine	m
r	Radial position of the rotor blade	m
u	Flow velocity	m/s
u_0	Incoming wind speed	m/s
u_{rel}	Relative velocity	m/s
u_{rot}	Rotational velocity	m/s
u_{tip}	Velocity at tip of blade	m/s
V	Volt	V
v	Kinematic viscosity	m^2/s

Greek characters

Symbol	Meaning	Unit
α	Angle of attack	°
γ	Yaw angle	°
λ	Tip speed ratio	[-]
ω	Rotational frequency	rad/s
ϕ	Pitch angle	°
ρ_{air}	Denisty of air	kg/m^3
θ	Twist angle	°

Abbreviations

Symbol	Meaning
35TA	Modified rotor blade
45TA	Modified rotor blade
AEP	Annual Energy Production
APP	Annual Power Production
BEM	Blade element momentum theory
CAD	Computer-Aided Design
CFD	Computational Fluid Mechanics
EAWE	European Academy of Wind Energy
GWEC	The Global Wind Energy Council
HVL	Western Norway University of Applied Science
LPTV	Lagrangian Particle Tracking Velocimetry
NTNU	University of Science and Technology
RANS	Reynolds-Averaged Navier Stokes
TI	Turbulence Intensity
TKE	Turbulent Kinetic Energy
VOI	Volume of Interest
VPM	Vortex Particle Method
VSC	Volume Self-calibration

1 Introduction

There is broad agreement amongst researchers and engineers that wind energy is one of the most promising energy technologies to accommodate the energy transition required to meet a greener future. The Global Wind Energy Council (GWEC) stated in their *Global Wind Report 2024* that 117 GW of installed capacity was installed during 2023. 106 of these GW were installed onshore, leaving 11 GW installed at sites offshore [1]. Tackling the technological challenges associated with wind turbines installed offshore, e.g. floating wind turbine technology, would be beneficial for energy production, as the potential for energy production is higher in areas located offshore. This is due to the increased velocity in the wind at sea, as well as a more frequent distribution of high-speed winds [2]. Wind turbines installed offshore will also avoid some human conflicts of interest related to onshore wind energy.

Seen from a Norwegian point of view, the government has ambitions of installing 30 GW of offshore wind capacity at the Norwegian continental shelf by 2030 [3]. This will include a mixture of both bottom-fixed and floating wind turbines.

Due to political restrictions, cable cost, maintenance and weather-dependent locations, wind farms are restricted to limited areas. Therefore, it is crucial to be able to utilize the wind's kinetic energy in the allocated areas in the most efficient way. Looking at wind energy in general, the turbine technology for a stand-alone wind turbine itself is already at an advanced level. However, wind turbines are rarely operated alone without any neighboring turbines in the vicinity, and when they are installed together in wind farms, there are several effects that limit the power production. One of these effects is the wind turbine wake, which is the motivation behind this experimental thesis.

Wake interactions are one of the main causes for increased fatigue loads and power production losses in wind farms. How to manipulate the wake's behaviour to benefit power production is still at an early stage, seen from a research point of view. Nevertheless, it can be assumed that the potential for improvements in these areas is going to influence how wind farms will be designed in the future. In fact, the potential of reducing the negative impact of the wake in wind farms is so great that the European Academy of Wind Energy (EAWE) made wake investigations a priority of their long-term wind energy research agenda [4].

A new and interesting approach for reducing the wake's negative impact on power generation is the *wake-diffusion rotor concept*. The concept patented by Equinor (2021) [5] aims to achieve a higher annual energy production (AEP) by letting the first row of wind turbines in a wind farm generate less power compared to the rest, so that more energy is available for the turbines installed downstream. To achieve this, different rotor geometries can be implemented to these front-row turbines by modifying the twist angle or chord length distribution. This can be referred to as *flow control* of the rotor blade, and will result in higher flow velocities in the center of the wind turbine wake. This will in turn result in increased shear gradients, accelerating the wake diffusion.

This thesis aims to further investigate the wake-diffusion rotor concept by conducting a lab-scale experimental test at MarinLab at the Western Norway University of Applied Sciences (HVL).

2 Theory

This chapter will shortly explain the theory related to wind energy used in this thesis. First, the physics associated with wind energy in a stream tube and over an airfoil geometry is listed. Then the BEM theory and rotor blade design is presented, before the wake flow and wind turbine interactions are described. Lastly, the relevant literature investigating the wake-diffusion rotor concept is presented.

2.1 Wind power

The power P_{wind} present in the wind blowing through a swept area A_{swept}, with an incoming wind velocity u_0, can be expressed as shown in Equation 1:

$$P_{wind} = \frac{1}{2}\rho_{air}A_{swept}u_o^3 \tag{1}$$

where ρ_{air} is the denisty of the air [6].

Wind turbines are designed to convert the kinetic energy in the wind into rotational movement of the turbine. However, it is not possible for a turbine to extract all the energy contained in the wind. Therefore, all turbines will have a power coefficient C_P, which is a dimensionless value that indicates how much of the theoretical power in the wind a wind turbine $P_{turbine}$ is able to extract. Equation 2 shows this.

$$C_P = \frac{\tau\omega}{\frac{1}{2}\rho_{air}A_{swept}u_o^3} = \frac{P_{turbine}}{P_{wind}} \tag{2}$$

where τ is the torque [Nm] and ω is the rotational frequency [rad/s] [6].

Thrust coefficient C_T for a wind turbine, which is a dimensionless value that indicates how much of the the thrust forces present in the wind that is acting upon the turbine, can be calculated as shown in Equation 3 :

$$C_T = \frac{F_T}{\frac{1}{2}\rho_{air}A_{swept}u_o^2} \tag{3}$$

where F_T is the thrust force that acts upon the wind turbine [6].

2.2 Airfoil design

The rotational velocity u_{rot} at a radial position r on the rotor blade is calculated as shown in Equation 4 [6].

$$u_{rot} = r\omega \tag{4}$$

The relative velocity u_{rel} that the airfoil section at distance r on the rotor blade experiences can be calculated as shown in Equation 5 [6].

$$u_{rel} = \sqrt{u_0^2 + u_{rot}^2} \tag{5}$$

An airfoil that is exposed to airflow will generate a lift force F_L and a drag force F_D that acts on the airfoil. This is due to the pressure difference between the upper and lower surface of the airfoil, created as the air flow split paths encountering the airfoil. The equation for the lift and drag forces are shown in Equation 6 and 7, respectively.

$$F_L = C_L A\frac{1}{2}\rho u_{rel}^2 \tag{6}$$

$$F_D = C_D A\frac{1}{2}\rho u_{rel}^2 \tag{7}$$

where C_L is the lift coefficient, C_D is the drag coefficient and A is the section area [6]. C_L and C_D are dependent on the airfoil's geometry and the Reynolds number, and are often found from dedicated experiments or simulations. A schematic illustration of an airfoil exposed to an incoming airflow can be seen in Figure 1.

The Reynolds number can be calculated as shown in Equation 8.

$$Re = \frac{inertia\ forces}{viscous\ forces} = \frac{ul}{v} \tag{8}$$

where u is the flow velocity, l is the length of the body and v represents the kinematic viscosity. The Reynolds number represents a dimensionless value that describes the relationship between the inertia and the viscous forces in a flow around a body [6], [2].

Tip speed ratio λ is defined as the relationship between the rotational velocity at the tip of the blade u_{tip} divided by the incoming wind velocity. This equation is shown in Equation 9 [6]:
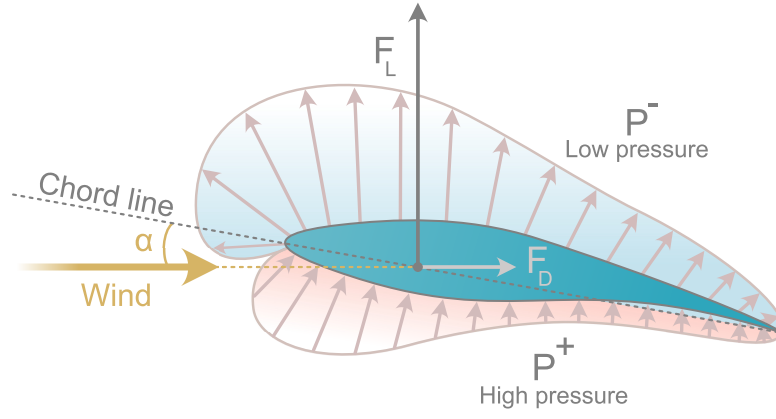
Figure 1: Schematic illustration of an airfoil. Inspired by [2].

$$\lambda = \frac{u_{tip}}{u_0} = \frac{\omega R}{u_0} \tag{9}$$

where R is the radius of the blade.

Figure 2 shows an inflow triangle at an airfoil section of a rotor blade. Here, the *chordline* is an imaginary line stretching from the leading edge to the trailing edge of the airfoil. Angle of attack α is the angle between u_{rel} and the chord line, twist angle θ is the angle between the chord line and the rotation plane and the pitch angle ϕ is the angle between the rotation plane and u_{rel} [6].
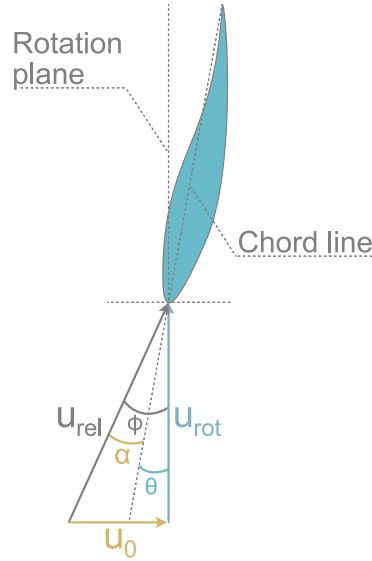
Figure 2: Schematic illustration of an inflow triangle at an airfoil of a rotor blade. Inspired by [2].

2.3 Blade element momentum theory

Blade element momentum theory (BEM) is a method that makes it possible to calculate steady loads, i.e. thrust and power as shown in Equation 1 and 2, for different wind speeds, rotational speeds and pitch angles. The method divides the rotor blade into several blade elements with a length dr and, through an iterative process, calculates the forces that acts upon each blade element. This is shown in Equation 10 and 11, respectively.

$$dF_n = \rho_{air} \cdot \frac{\omega^2}{2} \cdot l\left(r\right) \cdot dr \cdot (C_L \cos\phi + C_D \sin\phi) \tag{10}$$

$$dF_t = \rho_{air} \cdot \frac{\omega^2}{2} \cdot l\left(r\right) \cdot dr \cdot (C_L \sin\phi - C_D \cos\phi) \tag{11}$$

where $l(r)$ is the chord length at radial distance r. The normal and tangential forces dF_n and dF_t from the different blade elements are then separately added together and multiplied by the number of rotor blades present in the turbine. The resulting normal force is commonly referred to as the thrust force F_T, while the power of the turbine is calculated by multiplying the tangential force with the length of the radius and the rotational velocity at the tip of the blade, as shown in Equation 2. The normal force coefficient and tangential force coefficient can be calculated as shown in Equation 12 and 13, respectively [6], [2].

$$C_n = C_L \cos \phi + C_D \sin \phi \tag{12}$$

$$C_t = C_L \sin \phi - C_D \cos \phi \tag{13}$$

Prandtl's tip loss factor and *Glauert correction* are two correction factors that should be added to the method for more accurate results. The method, as well as the corrections, is described more in detail in [6].

2.4 Rotor blade design

While airfoil sections at the root of an airfoil blade are designed concerning stiffness and stability, the airfoil sections towards the tip of the blade are designed with focus on optimizing the aerodynamics performance [2]. The blade's performance is influenced by the geometrical blade parameters *twist angle* and *chord length*. When designing a blade for maximum performance, an airfoil section at a radial distance r on the rotor blade will have an optimal value for these parameters. The blade's twist angle is directly derived from the optimal flow angles at the different radial sections [4]. The radial chord length distribution can be designed by formulas presented by Glauert and Schmitz as shown in the work of Gerhardy [7]. Modifying either of these parameters will influence the blades overall performance.

2.5 Wind turbine wake flow

The wake of a wind turbine refers to the flow field behind the turbine. The flow field is a cone shaped volume with increased turbulence levels and reduced mean flow velocities. A schematic illustration can be seen in Figure 3.

A flow field containing turbulence refers to the chaotic movement of the particles in the flow field, and is the opposite of laminar flow, where the particles are organised in structured flow layers where their movement are highly predictable [8]. Turbulence can be quantified either as turbulence intensity (TI) or as turbulent kinetic energy (TKE). The equation for the latter can be seen in Equation 14.

$$TKE = \frac{1}{2} \left((u')^2 + (v')^2 + (w')^2 \right) \tag{14}$$

where u', v' and w' represents the average value of the three different velocity components of the average velocity fluctuation u_{rms}.

The wake can, roughly, be divided into three categories: *the near wake*, *the transition region* and *the far wake*. In the near wake, which typically is defined at an axial distance between $2 \leq x/D \leq 5$ downstream the turbine (D is the rotor diameter), the mean velocity in the center of the wake reaches a minimum at around $1 \leq x/D \leq 2$. This is a result of the different pressure gradients between the ambient flow and the wake region. In the near wake the wake expands, and its characteristics are dominated by vortices from the tip and root of the blade in the boundary layer that mixes with the higher velocity in the ambient flow. In the transition region, the vortices are decaying into turbulence, while the mean velocity in the wake keeps accelerating. In the far wake $> 5D$, the wake is fully developed and the rate of which the mean velocity at the center of the wake reaches the velocity in the ambient flow is dependent on the level of ambient turbulence. Experimental and numerical studies shows that there are only minor differences between the velocities within the wake and the ambient flow at distances larger than x/D=10. This means that the far wake usually dissolves at this distance, although the wake's presence has been observed at distances up to X/D=15 when the ambient turbulence level is significantly low [4], [2].

Although there are many fluid mechanic quantities that can be investigated in a wake flow, this thesis will focus on the mean stream-wise velocity u_{wake}.

2.6 Wind turbine interactions and wind farm control

Wind turbines arranged in wind farms typically have a spacing of $4 \leq x/D \leq 8$ between themselves. Larger separation distances between the turbines would be favorable for power production, but installation and cable costs keeps the turbine spacing from exceeding these limits. When arranged like this, the impact the turbines have on each other is inevitable. In the case investigated in the works of Barthelmie et al (2006) [9], an average power generation loss of 10% - 20% for the turbine installed downstream another was reported, reaching up to 35% for unfortunate wind directions. Work of Thomsen and Sørensen (1999) [10] shows that fatigue loads on wind turbines increased with 5% - 15% when they were installed in wind farms compared to a single free-flow wind turbine.
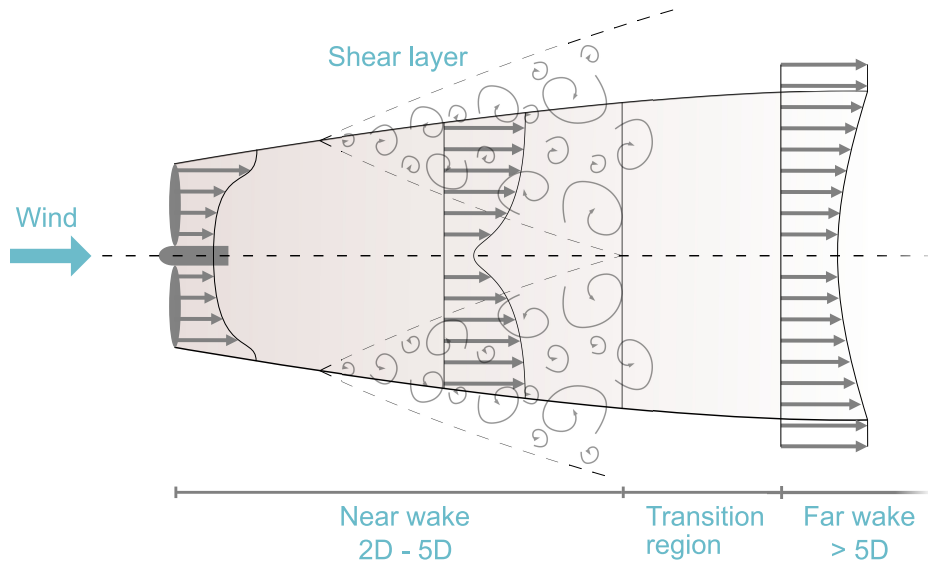
Figure 3: Shematic illustration of the wake flow behind a wind turbine. Inspired by Lissaman (1977) [4].

When designing future wind farms, both layout and rotor design should be considered. Especially for offshore installations, where the terrain is considered flat, a customized wind farm layout should be investigated. The aerodynamic interactions in wind farms investigated in the work by Sukhman (2023) [2] shows that an optimization of the wind turbine layout could potentially increase the APP with 0.12% - 0.64% over a period of one year in the different scenario investigated. Turbine rotors designed to leave more energy within the flow in a wind farm, could potentially benefit the overall power production of the farm [4].

Some state-of-art wind farm control systems, such as yaw and induction control, are implemented into the operation of wind farms to cope with unwanted contributions from the wake, and thereby maximize power production. Yaw control is used to intentionally misalign the wind turbine to the incoming wind. The wake will deviate from its normal course, steering out of path of the incoming wind for the turbine placed downstream [2]. This will shelter the downstream turbine from the wake, allowing it to generate more power. Induction control is used to pitch the blades so that the turbine generates less power. This will also allow the turbine placed downstream to generate more power [11].

As mentioned in Section 1, the wake-diffusion rotor concept is another approach for controlling the power production within a wind farm. It is a concept where the rotor blade has an outboard shifted thrust distribution [12]. To achieve this, the rotor blade geometry is modified at the root of the blade to intentionally convert less of the available energy from the upstream wind into rotational movement of the turbine. The flow around the different rotor blade sections are controlled, hence the expression flow control. The radial inducted rotor blades will result in a jet stream of high-energy wind in the center behind the turbine. The jet stream "ventilates" the wake, which again accelerate the wake diffusion [12]. A schematic illustration of the normal force distribution and the resulting velocity distribution for three different wake behaviours can be seen in Figure 4.

2.7   Research on wake-diffusion rotor concept

Although a lot of research on wind turbine wake, with the aim to quantify and understand its behavior, has been done, the wake-diffusion rotor concept is still uncharted territory.

The wake-diffusion rotor concept was first presented in Equinor ASA's patent (2021) [5]. The concept was further investigated numerically by Mordasov (2022) [12] and by Gerhardy (2024) [7]. Mordasov modelled three different wind turbine rotors, one of them representing the wake-diffusion rotor concept, using the RANS CFD software PyWakeEllipSys. RANS is short for Reynolds-Averaged Navier Stokes, and the method is described more in detail in [12]. The results from the RANS simulations done by Mordasov validate the claims made in the patent by Equinor ASA, resulting in an increased wind farm power generation by 3.8% and 2.5% for the wake-diffusion rotor concept in the different scenarios investigated. Gerhardys work investigate the impact that different twist angle distributions will have on the wake by modifying the NREL-5MW reference wind turbine using a vortex particle method (VPM). In Gerhardy's work, the wake-diffusion concept turned out to be the most promising of many rotor designs when aiming for a faster wake recovery [7].
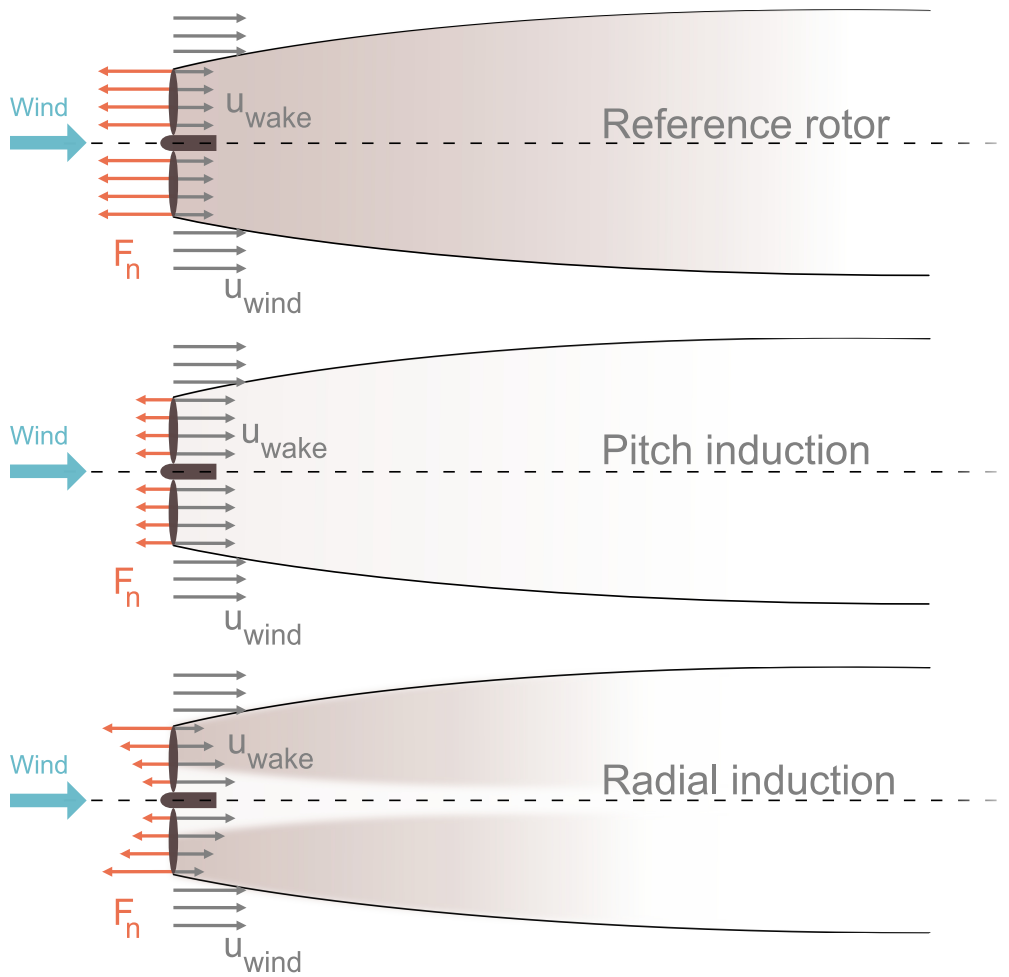
Figure 4: Schematic illustration of different wind turbine wake behaviour.

2.8 Motivation

The wake-diffusion rotor concept shows promising results when optimizing wind farms for maximum power production. The aim of this thesis is to use experimental methods to confirm the results by Mordasov (2022) [12] and Gerhardy (2024) [7]. High resolution images of the wake flow behind different model scale rotors will be produced, to get a better understanding of the flow physics in the wake behind such rotor concepts.

3   Methodology

In this chapter the methodology used in this experiment is described. The chapter will cover how the rotor blades are designed and manufactured, as well as a description of all the hardware and software used. The calibration process of the turbine's torque sensor and load cell, as well as the LPTV-system, is explained towards the end of the chapter, while the experimental setup and the post-processing of the recorded data closes it.

3.1   Rotor blade and turbine design

This section includes the method of which the reference rotor blades, the modified rotor blades and the turbine is designed. The various software that is used are described, as well as the manufacturing processes of all parts.

3.1.1   ForWind turbine

In order to share and compare experimental data with various research communities, the wind turbine design selected for this experiment is inspired by the model rotor design *ForWind*, which is a design that previously has been used in wind tunnel experiments conducted by Schottler et al (2018) [13] and Mühle et al (2018) [14] at Norwegian University of Science and Technology (NTNU) in Trondheim, Norway, and by Neunaber (2020) [15] and Hulsman (2022) [16] at University of Oldenburg, Germany, to name a few. The ForWind rotor is designed for low Reynolds numbers. The idea of having a standardised turbine design with the same rotor geometry could be a valuable basis for comparison amongst researchers in the wind energy community.

3.1.2   Reference rotor blade design

The rotor blade design for this experiments is based on the airfoil $SD7003 - 085 - 88$, which is the same airfoil incorporated in the ForWind design. The airfoil is chosen for its operation at low Reynolds numbers. The blade design measures 0.25m from the root of the blade to the tip. It is divided into 26 sections with $\Delta_{section}$ = 0.01m, where each section consist of an airfoil geometry, a chord length and a twist angle. These values are an identical replica of the ForWind turbine design. The innermost section of the blade is a circular section with $d_{circular}$ = 0.018m. At section 2 the airfoil $DU40$ is chosen to add strength and stability to the blade, as well as having an airfoil thickness large enough to accommodate the mounting piece that connects the blade and the hub. Between sections 2-6, the integrated function *Iterpolate Airfoils* in $QBlade$ (which is described in Section 3.1.5) is used to make a seamless transition from airfoil DU40 to the SD7003-085-88. Airfoil SD7003-085-88 is present from section 7 and all the way to the tip of the blade, which is section 26. Further in this rapport this blade geometry is referred to as the *reference blade*, and a detailed geometry of the blade can be found in Table 2 in Appendix A. An overview of all the different airfoils used in this experiment is displayed in Figure 5.
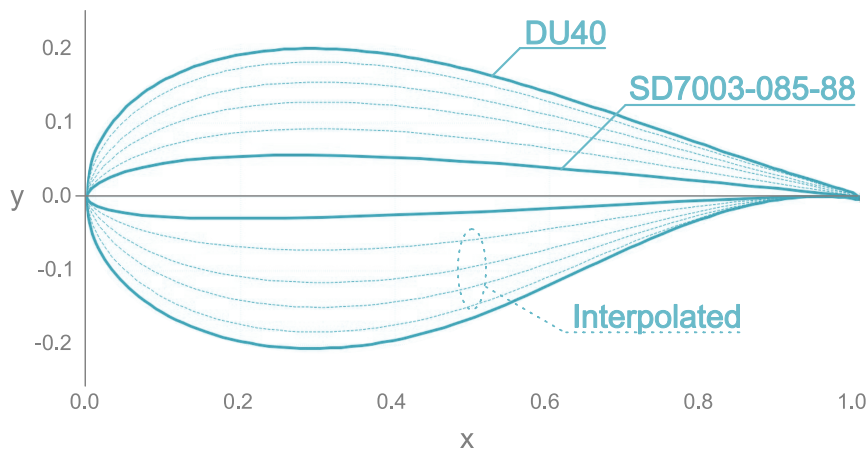
Figure 5: Overview of the different airfoils used when designing the rotor blades. DU40 (outer) and SD7003-085-88 (inner) are highlighted with a ticker line, while the interpolated airfoils are displayed in between.

3.1.3   Modified rotor blade design

The experiment aims to investigate the wake from different rotor designs. When a rotor blade is design for optimal power generation, it is the outer portion of the blade that has the largest power contribution [12], [5]. A potential small cost of

power production, by extracting less energy from the wind at the innermost sections of the rotor blade, could result in a quicker wake recovery and a greater power production within the wind farm. In order to investigate if a quicker wake recovery is achieved, two new rotor blades are designed and tested.

The modified rotor blades *35TA* and *45TA*, which stands for 35° and 45° twist angle, respectively, are designed and manufactured. The airfoils in section 1-13 of these new blades, i.e. $\frac{1}{26} \leq r/R \leq \frac{13}{26}$, have a larger twist angle compared to the reference blade. When investigating the innermost airfoil of the blade, the angel of attack is not longer optimal for lift generation. It is modified, so that little to none lift is generated. As mentioned, this will allow more energy to flow through the the rotor. The different twist angle distributions of the blades can be seen both graphically and photographic in Figure 6a and 6b. respectively.
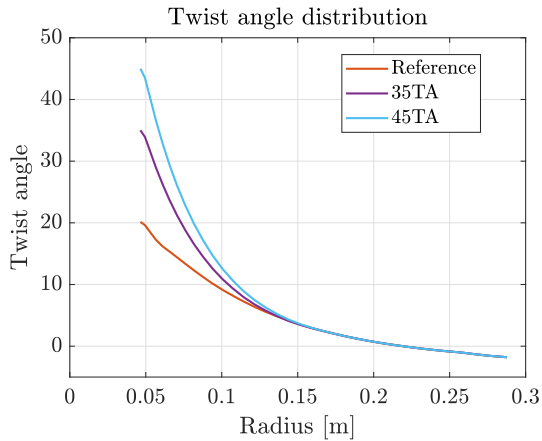

(a) Twist angle distribution.

(b) Picture showing the different twist angle distributions.

Figure 6: Twist angle distribution of the three different rotor designs.

3.1.4 Turbine design

When all three blades are connected to the hub, the rotor diameter of the turbine measures $D_{rotor} = 0.578$m, which means that diameter of the nacelle is $D_{nacelle} = 0.078$m. A detailed sketch of the rotor and a picture of the actual rotor used in this experiment is shown in Figure 7a and 7b, respectively.
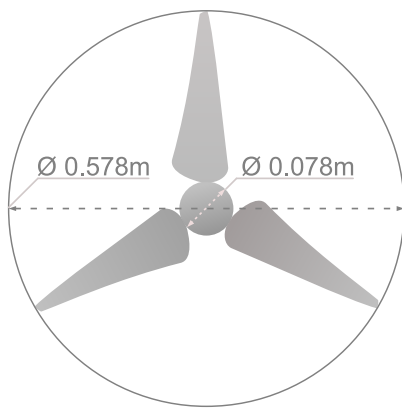
(a) Illustration of the rotor geometry.

(b) Picture of the rotor with all blades connected to the hub.

Figure 7: Illustration and picture of the rotor.

3.1.5 QBlade

The free and publically available software $QBlade$ is used for designing the different rotor sets. Airfoil and geometry data from Table 2 and 3 in Appendix A and B are implemented into the program to make a CAD sketch of the blade. This sketch is later exported and implemented in the software $Autodesk Fusion 360$, which is mention in Section 3.1.6. QBlade offers the possibility to perform BEM simulations of the different rotor sets. This function is utilized as the theoretical performance of each rotor design.

3.1.6 Autodesk Fusion 360

$Autodesk Fusion 360$ is a CAD program and is the software that has been used for designing all the parts that are used in this experiment. These parts include *hub mounting*, *hub cover*, *sensor cover* and the *connection piece between blade and hub*. Drawings of all the parts can be seen in Appendix E.

3.1.7 3D-printing

All the different rotor blades are manufactured with the same 3D-printer model Flashforge Adventurer 4. The printing material PLA+ is found to have the same structural qualities as the other materials tested, such as PLA and PLA CF (carbon fiber), and is the material used for all the blades. Autodesk Fusion 360 can save different file formats, such as *.stl*-file, which makes it easy to export the design to the 3D-printing software *FlashPrint 5*. In this program the setting $infill$ was set to 100% to make the blades as strong as possible. The blades are being printed one at a time, due to some irregularities in the surface finish when printing multiple blades at the same time. Printing time for one single rotor blade is approximately 6 hours and 30 minutes.

3.1.8 Milling

The mounting piece and the connection piece between the hub and the rotor blade are both manufactured in aluminium in HVLs workshop using two different milling techniques. This is done not just to add strength where there are the highest bending moments at the blade root, but also to ensure that the pieces will have a long life-span so that future experiments can be conducted with reliable parts. All of the milling is conducted by the mechanical engineers at HVL.

3.2 Experimental method

Three different approaches are commonly used when investigating the wake's behaviour. These include full-scale measurements, computational fluid mechanics (CFD) and experiments conducted in both wind tunnels and water tanks. The latter method is investigated in this thesis.

Both water and air behave like Newtonian fluids at low velocities [17]. This fact makes wind experiments conducted in water possible. Several experiments investigating a wind turbine wake, such as the work of Barber et al (2011) [18] and Kress et al (2016) [19], have previously been carried out in towing tanks.

3.3 Towing tank - MarinLab

The wake characteristics investigated in this experiment is conducted by towing the different rotor sets in HVL's MarinLab. MarinLab is a hydrodynamic research facility, situated at campus at HVL. The tank holds the dimensions 2.2m x 3m x 50m and is equipped with two towing carriages (master and slave) and six force-feedback flap-type wave paddles. More information about the MarinLab can be found at [20].

In this experiment the water tank is oriented such as the x-axis is running along the tank, y-axis is the depth and the z-axis is the width.

3.4 Turbine performance

In this section the turbine and the measurement devices, such as the torque sensor and the load cell, are described.

3.4.1 Turbine

The turbine used in this experiment is an already existing turbine. It is developed and manufactured in-house at HVL, and all of it components and dimensions are described more in detail in the work of Lande-Sudall et al (2023) [21].

In order to investigate different tip speed ratios, the turbine is equipped with a 200 W Maxon EC-i brushless motor, which also can act like a generator, in the nacelle. A picture of the turbine can be seen in Figure 8. The turbine has already been used in several experiments, and a short summary of its main objectives can be found in Table 1.

3.4.2 Torque and thrust measurements

The turbine is equipped with a torque-thrust sensor with a capacity of 5Nm and 100N, respectively. It is custom-made by Marin, Netherlands and is inspired by Dang et al (2012) [22]. A calibration of the torque sensor is performed. Figure 23 in Appendix D shows this.

For this experiment the rotor thrust signal was drifting, which means that a stable output signal during the calibration process was not obtained. Instead, a 50N s-beam load cell is installed at the top of the turbine, measuring the total thrust force induced on the turbine. The different thrust force contributions from the rotor, the nacelle and the tower is not

Figure 8: Picture of the turbine and the rotor sets.

Symbol	Parameter	Design
u_∞	Inflow speed	0.4 - 0.6 m/s
D_{tower}	Tower diameter	50 mm
D_{rotor}	Rotor diameter	578 mm
$D_{cacelle}$	Nacelle diameter	77 mm
$l_{nacelle}$	Nacelle length	760 mm
Q	Torque rating (sensitivity)	5 Nm (0.006 Nm/V)
T	Thrust rating (sensitivity)	100 N (0.23 N/V)

Table 1: Turbine parameters.

investigated individually, as the measurement that is going to be analyzed is not dependent on these individual values, but rather on the comparing one reference value to another.

A calibration of the s-beam load cell is performed prior to the measurement campaign, with results showing linear relation. This can be seen in Figure 24 in Appendix D.

3.5 Wake flow measurement with LPTV

Lagrangian Particle Tracking Velocimetry (LPTV) is used to measure the wake flow behind the turbine. This section will take a closer look the LPTV-system, the calibration process and the measurement procedure for this experiment.

3.5.1 LPTV-system

In this experiment the LaVision underwater LED-based Lagrangian Particle Tracking Velocimetry (LPTV) is used. This LPTV-system uses a new technique that includes white-light, and not laser light, to track tracer particles in the water flow for accurate volumetric flow measurements. The system consists of the MiniShaker multi-camera and the LaVision LED

Flashlight 300 illumination unit. The images captured with the MiniShaker multi-camera consists of 4 cameras, and they are placed in a fixed position with respect to each other, encapsulated in a cylindrical housing. All of the cameras are capable of capturing 8- or 10-bit images with a rate up to 510 frames per second, each and one of them with a resolution of 896x695 pixels. The light source illuminates an active area of 300mm x 100mm. LaVisions integrated software DaVis10 is used for capturing, analyzing and processing the data measured by the LPTV-system. A picture of the LPTV-system can be seen in Figure 9, and more information about the hardware of the LPTV-system used in this experiment can be found in [23] and [8].
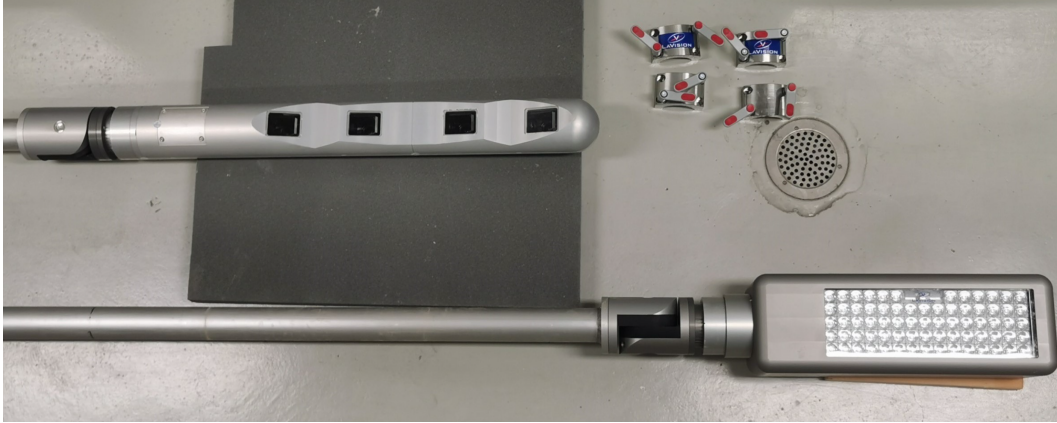

Figure 9: LPTV-system, consisting of the MiniShaker multi camera in the top left corner and the LED Flashlight 300 illumination unit at the bottom right corner. Picture from Eriksen (2023) [8].

3.5.2 Calibration

Prior to the volumetric flow measurement campaign, a perspective calibration of the camera system is conducted. In the first step of this calibration procedure, a 300mm x 300mm two-level calibration plate, with marker diameter of 3mm and marker distance 15mm, is imaged at five different positions along the z-axis, which is oriented along the width of the water tank, within the volume of interest (VOI). These z-positions are -100mm, -50mm, 0, 50mm and 100mm. The calibration plate is positioned such as the entire plate is visable within the camera frame. The calibration procedure allows the software to analyse 2 dimensional images from the four different cameras and, with great accuracy, reconstruct the movement of the tracer particles into a 3 dimensional flow field.

A Volume Self-calibration (VSC), which is a calibration feature within the DaVis 10 software, is the second step of the calibration procedure. VSC is an iterative process applied to 100 images of a recorded images and corrects for remaining optical distortions done in the first calibration step. More details about the VSC can be found in Wieneke (2018) [24] and Viola et al (2022) [23]. Within the software, the triangulation error is set to 2.5, with a maximum number of particles of 9.000. The resulting voxel disparity of < 0.1 is achieved, and is below the recommended lower-limit (≤ 0.1) for accurate flow measurement.

3.5.3 Measuring data

Due to previous experiment campaigns with the LPTV-system in HVL's MarinLab, the water tank is already contaminated with tracer particles. These are polyamide particles with a diameter of 100μ m. Before every measurement cycle with of the different rotor blades is performed, both the wave maker and a stirring device is used to ensure that the particles are properly mixed at the VOI.

In this experiments, the VOI captured from the LPTV-system is a rectangular volume of 0.25m x 0.45m x 0.09m. The camera unit and the light source is positioned such that the bottom half of the turbine is within the camera frame, with the nacelle being in the top of the picture frame while the rotor blades extend downwards. Due to the fact that the turbine radius $r_{turbine} = 0.289$m, the VOI is not large enough to include the volume beyond the wake's outer boundary. In order to compensate for this, both the camera unit and the light source are moved 0.2m down towards the bottom of the tank (y-axis) so that two image series, and also a larger VOI, are captured for each run. The two image series, at y=-1.225m and y=-1.425m, are then stitched together in the DaVis10 software with an overlap of 0.2m, resulting in a new VOI of 0.25 m x 0.65m x 0.09m.

The images in each run is captured over a period of 15 seconds with a frequency of 100Hz. This results in 1500 images, or samples per run. For each rotor set, distances at $2 \leq$ x/D ≤ 10, with an interval of x/D=1, at both y-positions are recorded, resulting in a total of 54 image series captured.

3.6 Experimental setup

For the experimental setup, the equipment is installed on both towing carriages and towed through the water tank with towing speeds ranging between 0.4m/s and 0.6m/s. This is well within the maximum capacity of the carriage, which is ~ 5 m/s. The turbine is installed on the foremost carriage (master), while the carriage in the back (slave) holds the LPTV-system. The depth of the water tank is, as mentioned, 2.2m and the center of the hub is positioned so that it is in the vertical center of the tank, 1.1m below the water surface. A schematic illustration of the experimental test setup is shown in Figure 10.
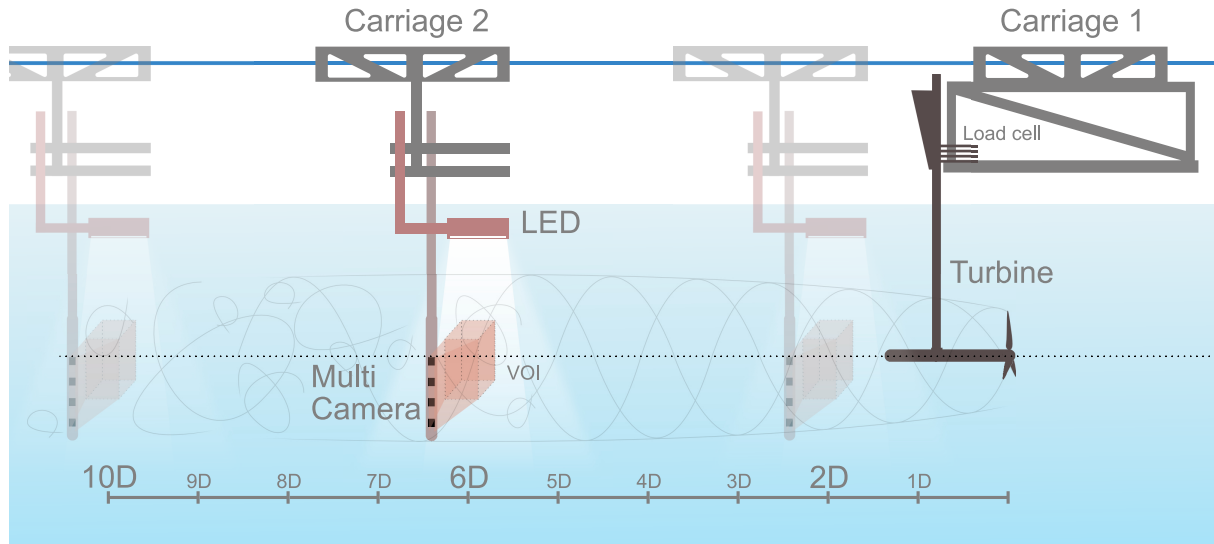

Figure 10: Schematic illustration of the experimental setup in HVL's MarinLab with the LPTV-system installed at distance x/D=6 from the turbine. LPTV-measurement at distances x/D=2 and x/D=10 are indicated.

3.7 Post-processing

This section shortly explains the post-processing procedure of analysing the data from the torque sensor, the load cell and the LPTV-system.

3.7.1 Torque and thrust measurements

All torque and thrust measurements are recorded via the *LabView* software, with a sampling frequency of 2kHz. The recorded data is converted into a *.txt*-file, which is then implemented to *Matlab* where all the data processing is done.

There are no forces acting on the turbine when it is still-standing in the water. Therefore, a zeroing of the torque sensor and the load cell is applied before a new rotor set is tested. This way any tension forces or unwanted noise is reduced, and the forces recorded while the turbine is running through the water is absolute.

Each measurement is recorded after the motor is engaged. The turbine is spinning at rest for approximately 10 seconds before the carriage is accelerated to target speed. The carriage is then running for 20 meters, before decelerating to a stand still. The motor is left running for a couple more seconds and the recording of the data stops. Before the carriage is moving, the torque sensor will experience "negative" torque due to the forces that acts upon the rotor when the turbine is rotating in still water. Since every measurement sequence consist of both accelerating and stopping the carriage, only the measurement from when the carriage is at a constant speed is processed. This is to avoid the contribution of the forces that occur in the non-steady states, as well as the ones that is present before the carriage is moving. A mean value from the cropped data is calculated, and a value for the torque- and thrust force at the given towing speed and tip speed ratio is defined. An example of how the cropping of the raw torque data is done can be seen in Figure 11. The same cropping method is applied to the thrust measurements.

3.7.2 LPTV-measurements

Images captured by the LPTV-system is post-processed using LaVision's software DaVis10. First, a combination of several spatial filters are applied to the raw images. The result of this is images where small-scale variations and noise are removed, as well as enhancing the contrast and increasing the sensitivity of the pixels. Further more, the Shake-The-Box process was applied to the images to visualize the particles movement in a volumetric flow field. The images captured at the two different y-positions mentioned in Section 3.5.3 are merged together with an overlap of 0.2m, resulting in a VOI
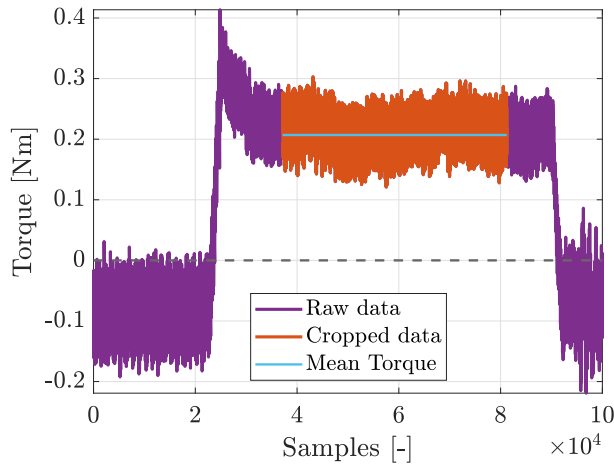
Figure 11: Example of cropping of torque measurements at $u_0 = 5.0$ m/s and $\lambda = 6.0$.

of 0.25m x 0.65m x 0.09m. The flow properties within the resulting VOI is then binned, which is a process that converts particle track to vector field data, measuring 96 x 96 x 96 in voxel size. This way, the VOI is divided into several smaller volumes which is the basis for the averaged values extracted when compiling the wake profiles. The post-processing procedure conducted in this experiment is inspired by the well documented post-processing procedure by Viola et al (2022) and by Eriksen (2023). More in-depth information about the procedure can be found in [23] and [8], respectively.

The LPTV-measurement campaign requires large amount of data to be stored. It also requires powerful computational resources in order to analyze the data in the post-processing procedure. Due to this, as well as limited access of time, the reader should be aware of the simplifications made to be able to evaluate preliminary results.

Only 50 samples out of 1500 is being analysed. Although this may appear as a large amount of data being omitted, the work of Eriksen (2023) [8] shows that similar mean velocities in the center of the wake are achieved when comparing measurements containing various number of samples (from 400 to 2400) were used. Still, analyzing 50 samples, which translate to half a second out of 15, drastically reduces the quality of the measurements. This particularly affects the TKE-measurements, at which significantly longer time series is required for achieving accurate results.

The wake's characteristics are evaluated at distances x/D=2, x/D=6 and x/D=10D. Even though more distances would lead to a more comprehensive wake characterisation, these distances are a good representation of the different behaviours of the wake throughout it's length, covering the three phases explained in Section 2.5.

The wake measurements are conducted on the bottom half of the turbine. In order to emulate the full size of the wake, the upper part is a mirrored projection of the measurements at the bottom half.

3.8 Measurement uncertainty

There are mainly two measurement uncertainties associated with experimental trials. These are systematic error and random error. A systematic error could be an error that is present in the measurement system used, such as a none-calibrated caliper, resulting in an error of similar magnitude if repeated throughout different measurements. A systematic error could also be a result of environmental factors, as well as observational ones [8]. Random error refers to independent conditions in which the measurements are being conducted. Random errors are unforeseen and might be difficult to control, but preventive measures like acquiring larger amounts of data will help reducing its significance [25].

Although procedures preventing all conceivable uncertainties associated with this experiments are carried out, there will inevitable be some uncertainties related to the measurement campaigns. This section will highlight the measurements uncertainties associated with this experiment without going into detail in which precautionary measures conducted. It should be noted for the reader that due to limited access of time, a precision error analysis is yet to be performed in this experiment.

3.8.1 Torque and thrust measurements

The calibration of the torque sensor and the load cell decreases the amount of systematic error present in the measured output values. An other systematic error such as oscillation of the tower when it's installed on the moving carriage during the measurement campaign could result in inaccurate torque and thrust measurements. Further more, a third systematic error could be that zeroing both the load cell and torque sensor before a measurement campaign could potentially be executed while there still is some tension force present.

One potential random error could be that some vibrations from the wiring system that is towing the carriages could interfere with the load cell measurements. Another one is that the MarinLab is equipped with various electronic devices that could potentially affect the measurements.

A precision error for the torque and thrust measurements could be calculated by repeating measurements. This is an comprehensive process, and due to limited access of time, this is yet to be done.

3.8.2 LPTV measurements

A potential systematic error is that the MultiShaker camera is manually adjusted between two different positions between the measurement runs, and a small change in both angle and height, in which the camera captures the VOI, is possible. Another one is that the concentration of tracer particles throughout the water tank could vary, which again can lead to inaccurate results. Further more, turbulent conditions in the water might be present before a new measurement is being conducted. One last systematic error worth mentioning is that reflections from other light sources can interfere with the illumination setup.

A precision error for the LPTV-measurements is a complex procedure and a topic of current research. A good review of the procedures is formulated in the work of Sciacchitano (2019) [26]. Due to limited access of time, this has not yet been done for the LPTV-measurements.

4 Results and discussion

The aim of this thesis is to investigate whether a faster wind turbine wake recovery is achieved by modifying the rotor blades such that they have an outboard shifted thrust distribution, as well as to determine how the potential power production is affected for a turbine placed downstream another one.

This chapter first evaluate the outcome of the BEM simulation conducted in QBlade. Further more, the results from the experiments carried out at HVL's MarinLab, including both turbine performance and wake profiles, are presented and discussed.

4.1 Power and thrust from BEM analysis

Although this is an experimental study, results from the BEM simulation conducted in QBlade are presented in this section to set a theoretical reference value for the different rotor designs.

4.1.1 Evaluation C_P and C_T from the BEM analysis

The C_P-values for all the different rotors, as displayed in Figure 12a, show similar result, registering the largest disparity at $\lambda > 6$. The C_T-values in Figure 12b are showing the same tendency, registering disparity for $\lambda > 4$. In this region, i.e. $\lambda > 4$, the reference blade holds the highest C_T-values, which means that it is the rotor that experience the largest thrust force. When investigated closely, the graph also shows that the 35TA obtain slightly higher C_T-values compared to the 45TA. This is a promising observation concerning a faster wake recovery, since it's dependent on the force acting upon the rotor blade.
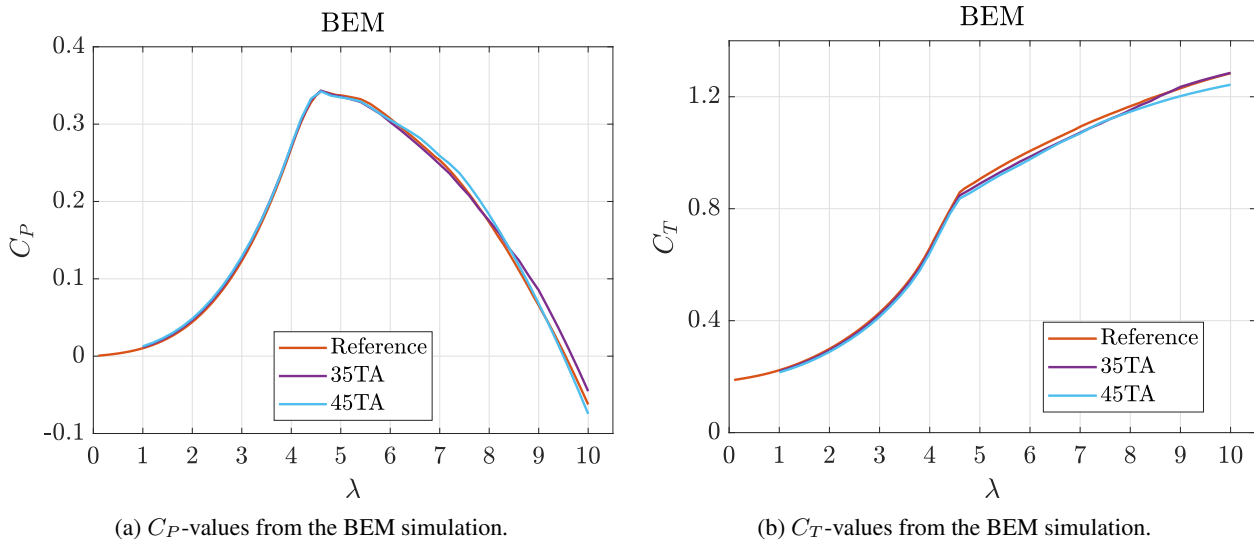

(a) C_P-values from the BEM simulation.

(b) C_T-values from the BEM simulation.

Figure 12: C_P and C_T from the BEM simulation for the three different rotor designs conducted in QBlade.

4.1.2 Evaluation C_n and C_t from the BEM analysis

Even though only minor differences regarding C_P and C_T-values between the different rotor designs are observed in Figure 12, the normal force- and tangential force coefficients C_n and C_t, respectively, displayed Figure in 13, show the effect that the modified rotor blade geometry has. The disparity in the normal force coefficient distributions between $0.0385\text{m} \leq \text{r} \leq 0.15\text{m}$ is a result of the outboard shifted thrust distribution for the modified rotor blades, as stated in Section 2.6. Disparity in the tangential force coefficients is also present, with the greatest disparity between $0.0385\text{m} \leq \text{r} \leq 0.075\text{m}$. This indicates that less energy is being converted in this region of the blade, as intended for the wake-diffusion rotor concept.

The sudden peak in C_n and C_t-value for 45TA at r $\sim 0.05\text{m}$ is likely to be caused by the BEM simulation not converging for the inner blade elements. This is a known numerical problem for BEM simulations in off-design conditions, and it is not investigated any further.

4.2 Power and thrust coefficients from measurements

Before the wake measurements can be carried out, it is necessary to collect and evaluate performance data from the different rotors, i.e. C_P and C_T, as well as to test whether the blades are strong enough to withstand the forces that they are exposed to. The aim of this is to find a flow velocity and a 'best performance' tip speed ratio that is close to the

(a) C_n-values from the BEM simulation.

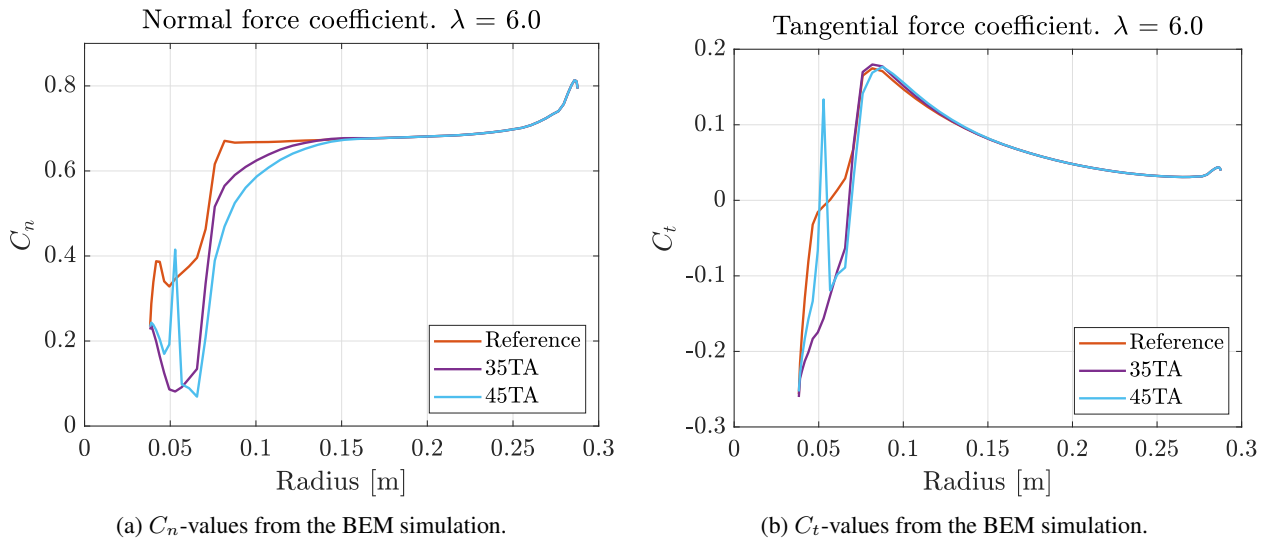(b) C_t-values from the BEM simulation.

Figure 13: C_n and C_t from the BEM simulation conducted in QBlade.

theoretical values simulated in the BEM-simulation, which in turn can be utilized when conducting LPTV-measurements at a later stage.

4.2.1 Reference rotor performance

The reference rotor is the rotor that theoretically is exposed to the greatest forces, and therefore this rotor is selected when measuring the forces that act upon the rotor at three different towing speeds, 0.4m/s, 0.5m/s and 0.6 m/s. C_P-values, as well as C_T-values, for each run can be seen in Figure 14.
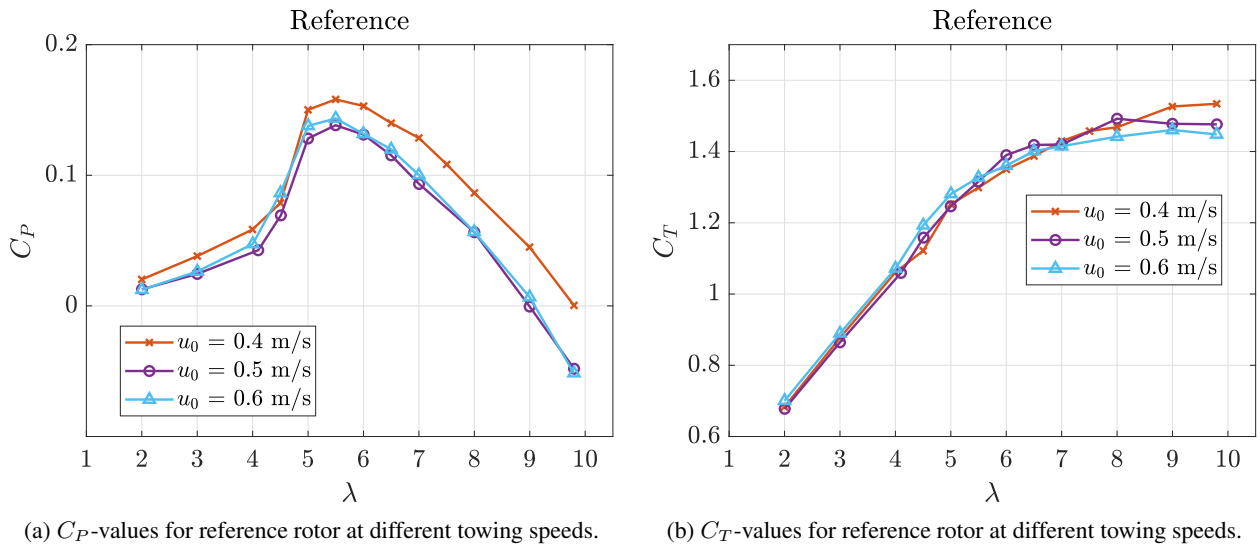

(a) C_P-values for reference rotor at different towing speeds.

(b) C_T-values for reference rotor at different towing speeds.

Figure 14: C_P and C_T-values from the reference rotor.

A slightly higher C_P-value is measured for the reference blade at u_0=0.4m/s. Although this value in theory should not differ from the values measured at u_0=0.5m/s and u_0=0.6m/s, some abnormalities in the measured values are expected when conducting experiments. Possible explanations for C_P-values at u_0=0.4m/s could be caused by a systematic error explained in Section 3.8.1. Nevertheless, the curves clearly indicates Reynolds-independent trials.

Disregarding the slightly elevated C_P-values at u_0=0.4m/s, matching values are obtained for λ=6.0. Due to this, and the fact that Schottler et al (2018) [13] and Mühle et al (2018) [14] has previously done wake measurements behind the same rotor geometry (ForWind) at λ=6.0, a tip speed ratio λ=6.0 and towing speed of 0.5m/s is chosen as the design point for the LPTV-measurement campaign. Choosing a lower towing speed than 0.6m/s also reduces the amount of bending that the rotor blades are exposed to.

4.2.2   Comparison reference rotor performance with BEM simulation

Figure 15 shows the experimental values for C_P and C_T compared to the values generated by BEM simulation in QBlade. The obvious disparity in C_P-values in Figure 15a is a case investigated thoroughly throughout both the experiment and post-processing campaign, without resulting in any obvious explanations. The measured torque from the torque sensor shows, for some inexplicable reason, only half of the expected value, resulting in lower C_P-values regarding turbine performance. Nevertheless, disregarding the measurements from BEM, the C_P-values from the turbine performance at the different towing speeds 0.4m/s, 0.5m/s and 0.6m/s are matching one another. A general observation for the three different C_P-curves from the reference rotor is a lower tendency in the power performance between $2 \leq \lambda \leq 4$, and a slightly steeper gradient between $4 \leq \lambda \leq 5$, when comparing the performance to the BEM simulation. One suspicion is that this could be a systematic error resulting in flow release due to low Reynolds numbers for these λ. This will be further investigated.

As mentioned in Section 3.4.2, the thrust force measured in the load cell is the result of the three different thrust contributions. They are from the rotor, the nacelle and the tower, and therefore higher C_T-values compared to the BEM simulation is achieved. Although one could investigate the magnitude of each of the different contributions, it is not needed in order to draw the conclusion that the C_T-values measured in this experiment is as expected based on the theoretical calculations.
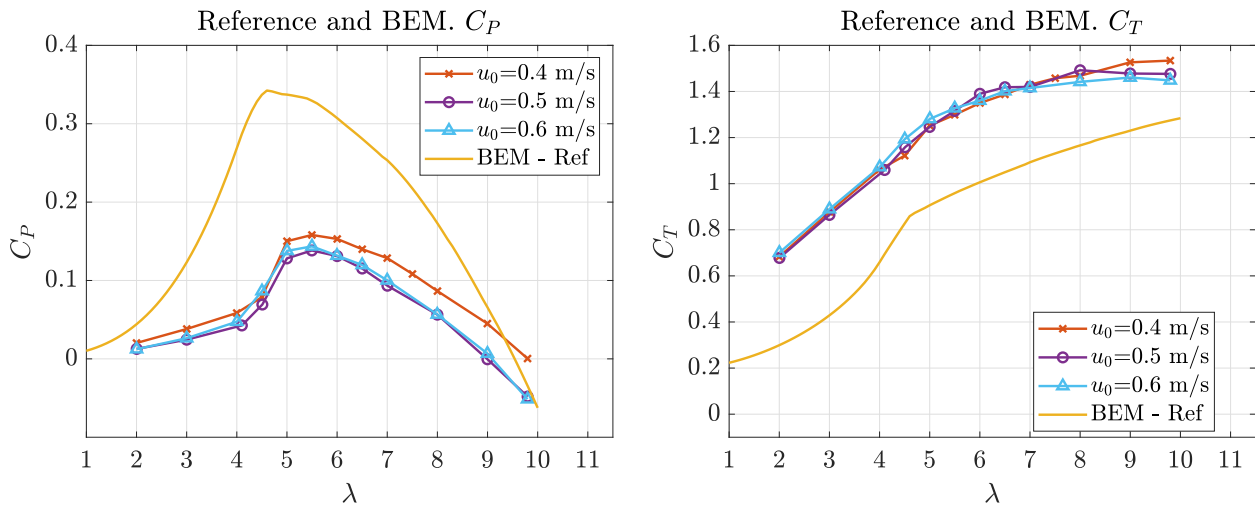
(a) C_P-values from the measurements and the BEM simulation.   (b) C_T-values from the measurements and the BEM simulation.

Figure 15: C_P and C_T-values for the different rotors at 0.5 m/s.

4.2.3   Comparison C_P and C_T-values for the reference and 35TA at u_o=0.5m/s

Figure 16 shows the C_P and C_T-values for the reference and 35TA at the experimental design points. The measurements from the 45TA was deviating too much to be included in this graph. However, it is expected that the C_P-curve from the 45TA should look similar the to ones present, which matches each others values. The 35TA clearly show lower C_T-values compared to the reference rotor, as on could expect. This is due to reduced loading in the center of the rotor.

4.3   Wake flow measurements

This section takes a closer look at the LPTV-measurements conducted in this experiment. All measurement from the LPTV-system is done by following the procedure given in Section 3.5.3, in addition to adhering to the simplifications that have been made in Section 3.7.2.

4.3.1   Velocity profiles at x/D=2

A graphic representation of the wake's mean stream-wise velocity profile in the different wind turbine wakes produced at distance x/D=2 from the different rotor designs is presented in Figure 17. On the y-axis, y/D represents a dimensionless value, placing the center of the turbine at y/D=0, while the tip of the rotor blades tangent a swept area located between -0.5 ≤ y/D ≤ 0.5. The x-axis is also representing a dimensionless value, 1 - u_{wake}/u_0, where higher velocities $\sim$ 0.5m/s results in a value $\sim$ 0, and lower velocities $\sim$ 0.0m/s results in a value $\sim$ 1. At first glance, the results in Figure 17 indicates that higher velocities in the center of the wake is achieved for 35TA and 45TA. This corresponds to the modified radial blade sections and is an expected observation. Another expected observation is that similar velocities towards the the outer part of the wake is observed. This corresponds to outermost portion of the rotor blade, which is not modified.

17

(a) C_P-values for the different rotors at 0.5 m/s.
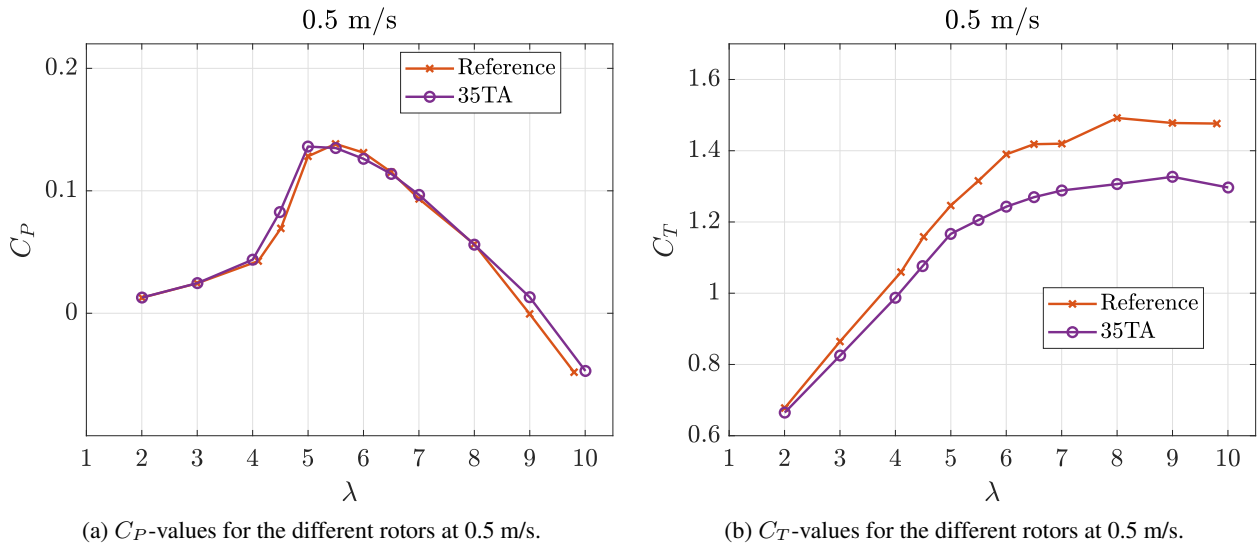
(b) C_T-values for the different rotors at 0.5 m/s.

Figure 16: C_P and C_T-values for the different rotors at 0.5 m/s.

This is a strong indication that the velocity profiles for the wake at this distance could be a good representation of the actual characteristics of the wake. To further investigate the quality of the measurements, a comparison with other studies is discussed in Section 4.3.2 and 4.3.3.
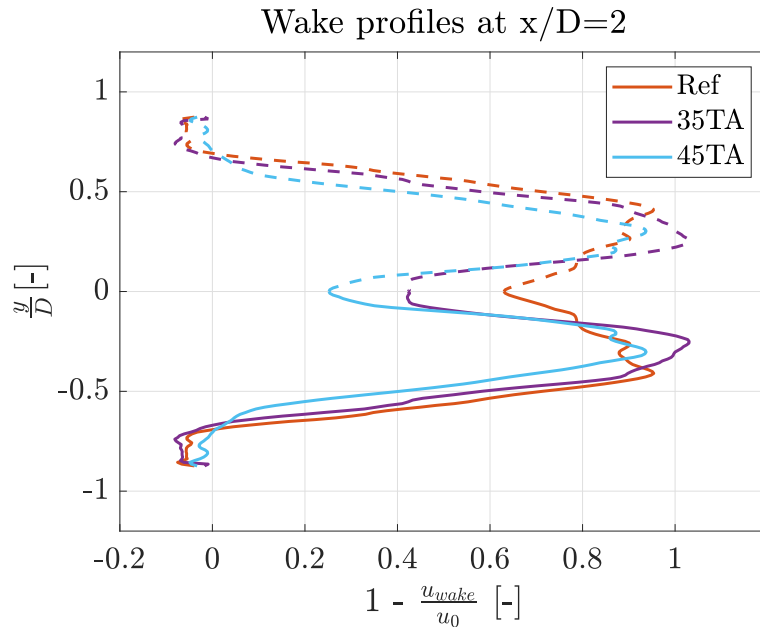

Figure 17: Wake profiles produced by reference, 35TA and 45TA at x/D=2.

4.3.2 Comparison ForWind rotor design with reference rotor

As mentioned in Section 3.1.1, both Neunaber (2020) [15] and Hulsman et al (2022) [16] conducted experiments with the ForWind rotor design in the wind tunnel at Oldenburg University, Germany. Figure 18 shows a graphic representation of the findings in their work compared to the reference rotor, which is also heavily inspired by the ForWind design. Although lower velocities at the region around the tip of the blade is registered for the reference rotor, the tendencies in which the wake is portrayed is clear.

Present in Figure 18 are now three different wake profiles which originates from the same rotor design, from 3 independent studies, showing similar results. This is a strong indication that the wake measurement from the reference rotor conducted in this experiment at distance x/D=2 is a good representation of the wake formation, even though the measurements are based on few samples.
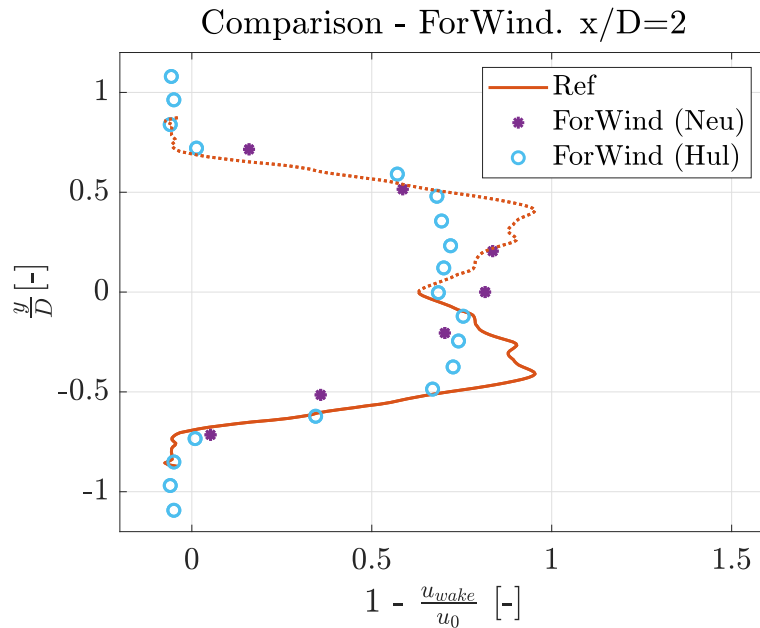
Figure 18: Wake from the reference rotor compared to the the wakes from the ForWind rotor found in the experiments conducted by Neunaber (2020) [15] and by Hulsman et al (2022) [16] at Oldenburg University.

4.3.3   Comparison rotor designs from Equinor ASA patent with reference, 35TA and 45TA at x/D=2

To further evaluate the accuracy of the velocity profiles produced by the 35TA and 45TA at x/D=2, a quantitative comparison between the reference, 35TA and 45TA and the 3 different rotor designs, Ref, $Vent1$ and $Vent2$ respectively, investigated in the Equinor ASA patent [5] is made. The rotor design Ref is optimized for maximum power production at λ=6.0, whereas Vent1 and Vent2 are designed with the goal of achieving a ventilated wake center, just as 35TA and 45TA are. Although the rotor geometry of the rotors used in Equinor's patent [5] is not comparable with the rotors used in this experiment, the basis for how the experiment is set up show similarities. The comparison is displayed in Figure 19. Disregarding the obvious disparity in the magnitude of the mean velocities, similar tendencies are observed in the two different scenarios. Both of them clearly show that higher mean velocities is present in the center of the wake from the modified rotor blades, which in turn confirms that a ventilated wake center is achieved.

A similar indication as the one drawn from Section 4.3.2, regarding the accuracy of the reference rotor wake at x/D=2, could also be valid for 35TA and 45TA at the same distance, based on the comparison made in Figure 19. This means that all three wake profiles shown in Figure 17 in Section 4.3.1 are a good representation of the wakes that is produced at this distance.

4.3.4   Wake profiles at x/D=6 and x/D=10

Figure 20a and 20b display the measurements at distance x/D=6 and x/D=10, respectively. As mentioned in Section 2.5, a fully developed wake with some velocity disparity, forming a Gaussian shaped wake profile, is expected at x/D=6. Although both the reference and the 35TA showing similar tendencies in the outer wake and in the ambient flow, the measurements are fluctuating. It is also noted that the wake produced by the reference rotor holds a higher mean velocity at the center of the wake when compared to the 35TA. This should not be the case, as the 35TA ventilates the wake, accelerating the velocity in the center, as seen in Figure 17. Regarding the measurement for the 45TA, it clearly deviates from its expected behaviour, as well as from its neighboring curves.

Gerhardy's work [7] investigated the wake characteristics behind the reference wind turbine NREL 5MW numerically by testing various blade geometries, amongst them a reference blade and a blade designed with an outboard shifted thrust distribution, at λ=7.0. Gerhardy's findings at distance x/D=7, which is close to the distance investigated in Figure 20a, clearly shows that a higher mean velocity was achieved throughout the volume of the wake when comparing the modified rotor blade with the reference blade. This is not the case for the observations done in Figure 20a.

The measurements at x/D=10 in Figure 20b is also deviating from its expected values, displaying fluctuating and unexpected wake profiles. Gerhardy also made a comparison of the mean velocity in the wake produced by the reference rotor and the modified rotor at x/D=9. It showed similar velocity disparity as the one described earlier. The measurements in Figure 20b show that the wake produced by the 35TA is unrealistically accelerated in the center of the wake compared to the distance x/D=6. The velocity profiles from the reference and the 45TA continue to hold a wave-like shape.
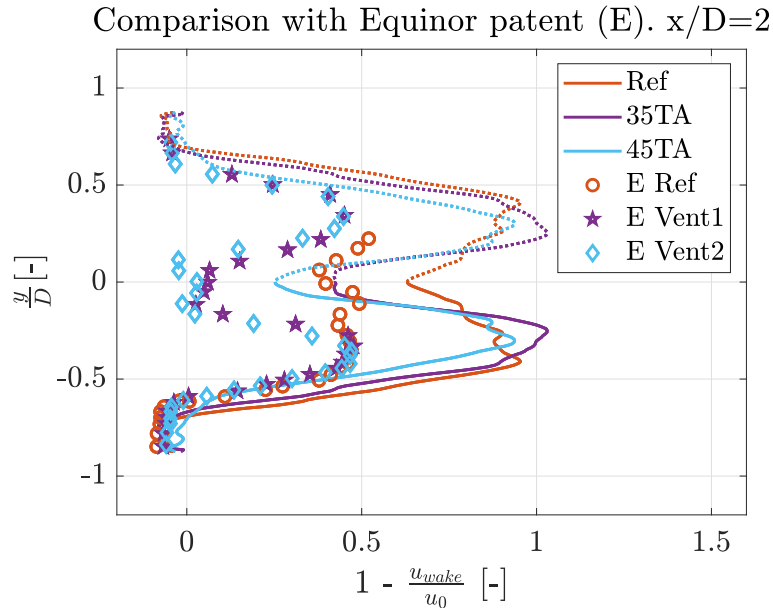
Figure 19: Comparison of the wakes produced in this experiment to the wakes investigated in the Equinor ASA patent [5].
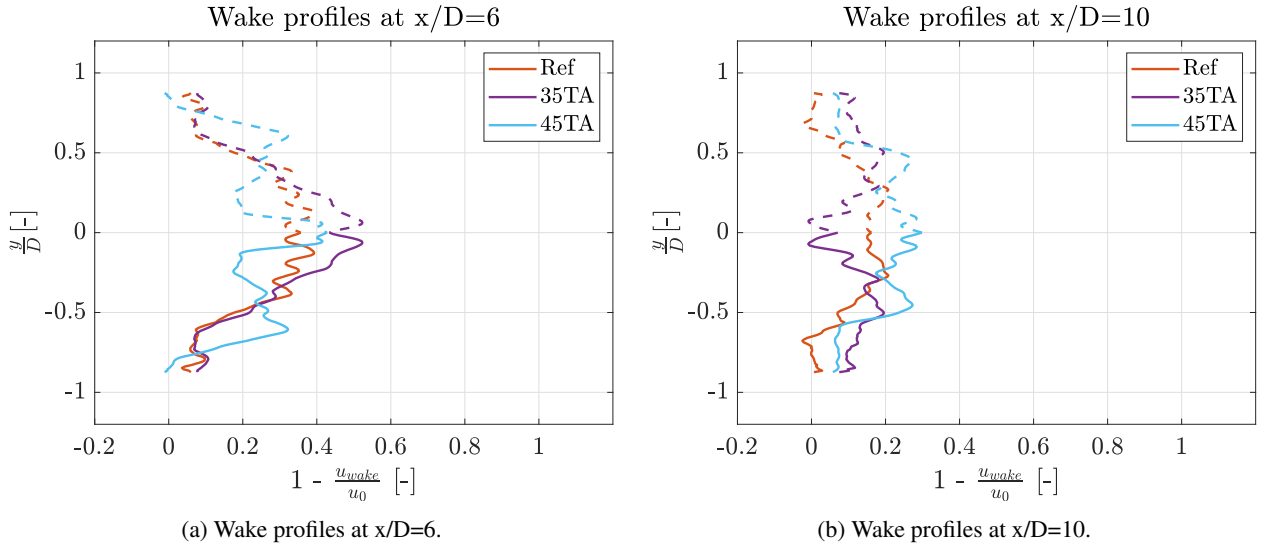

(a) Wake profiles at x/D=6.

(b) Wake profiles at x/D=10.

Figure 20: Wake profiles from reference, 35TA and 45TA at x/D=6 and x/D=10

4.3.5 Rotor-averaged wake velocities

The mean velocity in the wake behind the turbine at distances x/D=2, x/D=6 and x/D=10 is shown in Figure 21. It is calculated by taking the mean of every velocity measured from the center of the rotor to the tip of the blade along one profile-line consisting of 56 measurement points.

The rate at which the wake recovery is greatest is in the near wake, registering the highest velocity disparity at distance x/D=2D. Although the velocity disparity registered at this distance is of little concern to potential energy producers, the effect of a faster wake recovery takes on greater significance further downstream. At distance x/D=6.0, which is, as discussed in Section 2.6, a typical spacing between two neighboring wind turbines installed in a wind farm, the average velocity measured in the wake is highest for the 45TA. In the numerical results in the work of Mordasov [12], a velocity disparity at similar distance, i.e. x/D=5, of Δ_{u_{wake}/u_0}=0.04 was achieved when comparing the the mean velocity from the two rotor designs that differ most from each other, resulting in a theoretical power production increase of 18 % for a wind turbine installed downstream another turbine. A similar approach calculating the potential power production for a turbine installed downstream at distance x/D=6 in this experiment, is shown in Equation 15. As mentioned in Section 2.1 in Equation 2, the power produced by a wind turbine is proportional to its incoming velocity cubed, $P_{turbine} \propto u_0^3$. Thus, due to the velocity disparity between the 45TA and the reference, the potential increase in power production by a turbine placed at distance x/D=6.0 downstream another turbine is 28.9%, as Equation 15 shows [12]. It should be noted to the reader that the calculation done in Equation 15 is only to show the potential increase in power production achieved
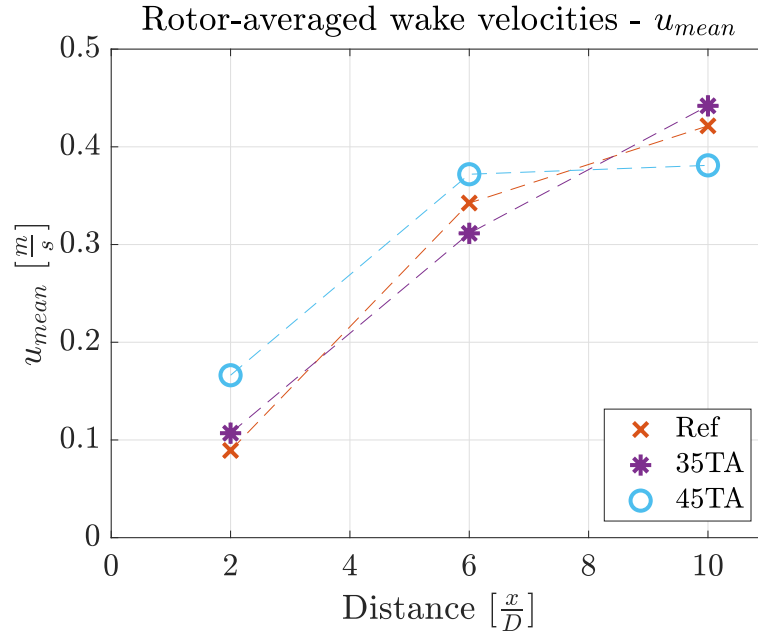
Figure 21: Comparing the mean velocity at x/D=2, x/D=6 and x/D=10. The dashed lines are only displayed to graphically connect two measuring points, and are not a representation of the mean velocity in between.

by having a higher mean velocity in the wake, and that the data which the calculation is based on is not sufficiently good enough.

$$\frac{P_{45TA}}{P_{ref}} \propto \left(\frac{u_{mean,45TA}/u_o}{u_{mean,ref}/u_0}\right)^3 = \left(\frac{\frac{0.37m/s}{0.5m/s}}{\frac{0.34m/s}{0.5m/s}}\right)^3 = 1.289 \tag{15}$$

Further more, the results show high velocity disparity at x/D=10. At this distance, the wake should be close of collapsing, resulting in mean velocities ~ 0.5 m/s.

Although a direct comparison between the velocity disparity achieved at x/D=5 by Mordasov and the ones measured in this experiment is unfair, a similar tendency regarding the velocity disparity between the reference rotor and the modified rotors is expected. This is, yet again, an indication that the measurements at x/D=6 and x/D=10 is not sufficiently good enough.

4.3.6 Evaluating wake profiles at x/D=6 and x/D=10

When comparing the wake profiles in Figure 17 and 20, increasing velocity profiles are observed, as well as the tendencies described in Section 2.5. Still, the measurements at x/D=6 and x/D=10 deviate from the expected values. This supports the assumptions made by evaluating Figure 20 and 21 that the data from the LPTV-measurement campaign is analyzed using not enough samples at this point.

5 Conclusion

In this thesis a wind turbine rotor wake's characteristics from modified rotor blade designs are investigated. Two modified rotor sets, each of them having a modified twist angle distribution at the innermost half of the blade, are compared to a reference rotor set which is designed for optimal power production. The experiment is conducted at HVL's MarinLab, where the rotors are towed through the water tank. Turbine performance is measured using an in-house turbine developed at HVL, while the flow field in the wake is recorded using a LPTV-system. Downstream distances are investigated for each rotor set and the mean velocity in the wake is compared.

The thesis contributes to the on-going research on wind turbine wakes by evaluating the wake's behaviour using an experimental method. At the nearest distance investigated, it shows similar results to those found in the numerical studies done by Mordasov [12], Gerhardy [7] and measurements documented in the Equinor ASA patent [5]. This is achieved by modifying the blade geometry at the innermost half of the rotor blade, and thereby intentionally converting less of the available energy in the wind, which will lead to increased mean velocities at the center of the wake at distance x/D=2. In this respect, the wake measurements at this distance show that the wake-diffusion rotor concept is a promising concept for potentially increasing the annual power production of a wind farm. Measurements at distances x/D=6 and x/D=10 are currently being processed to investigate the influence on the wake's recovery at larger downstream distances.

The thesis outlines the potential extensions in future studies to further investigate the preliminary results conducted in this experiment, in addition to propose alternative methods and experimental setups.

Future work will include more samples when post-processing the data from the LPTV-system to more accurately reconstruct the wake flow. The amount of samples analyzed will in addition be sufficient enough such that the turbulent normal and shear stresses in the wake can be analysed. Also, a more comprehensive wake profile, containing measurement data from all the distances ranging from $2 \leq x/D \leq 10$, will result in a more nuanced mapping of the the wake characteristics from the three different rotor blades.

Different twist angle distributions could be investigated to compare if similar tendencies are achieved regarding the wake-diffusion rotor concept. Another flow control parameter not investigated in this experiment is the chord length distribution, which also could be an interesting topic of investigation. More in general, future work conducting computational fluid dynamic analysis of the different rotor designs could be performed to compare simulated results against experimental ones. Additionally, an experimental setup measuring the power production of two turbines, where one is located downstream of the other, at different distances would be a highly interesting study to conduct.

The insights gained from this work has led to a deeper understanding of the impact of rotor blade geometry on wind turbine wakes, and in turn on power production. The findings in this thesis pave the way for further optimisation of wind farms, so that wind resources can be utilised in the best possible way in the future.

References

[1] Global Wind Energy Council. Global Wind Report 2024. Retrieved from: https://gwec.net/global-wind-report-2024/ Accessed 29.04.2024.

[2] D. Sukhman. Investigation of aerodynamic interactions in the wind farm and their influence on the power output. February 2023. MSc thesis. TU Braunschweig.

[3] Olje og ernergidepartementet. Den norske regjeringen, December 2023. Retrieved from: https://www.regjeringen.no/nn/tema/energi/landingssider/havvind/id2830329/ Accessed 2024.04.29.

[4] F. Mühle. *An experimental study on rotor-wake interactions of wind turbines*. PhD thesis, September 2018. NMBU.

[5] Equinor ASA. US Patent for: Rotor blade shaped to enhance wake diffusion. Patent # 10,975,837. April 13, 2021 - Justia Patents Search.

[6] M. O. L. Hansen. *Aerodynamics of wind turbines*. Earthscan, 2nd edition, 2008. OCLC: ocm86172940.

[7] F. B. Gerhardy. Wind Turbine Blade Optimization for Minimizing its Wake's Footprint. April 2024. MSc thesis. TU Braunschweig.

[8] T. Eriksen. Flow measurements in the wake of multirotor wind turbine arrangements. June 2023. MSc thesis. University of Bergen.

[9] R. J. Barthelmie, G. C. Larsen, S. T. Frandsen, L. Folkerts, K. Rados, S. C. Pryor, B. Lange, and G. Schepers. Comparison of Wake Model Simulations with Offshore Wind Turbine Wake Profiles Measured by Sodar. *Journal of Atmospheric and Oceanic Technology*, 23(7):888–901, July 2006. Publisher: American Meteorological Society Section: Journal of Atmospheric and Oceanic Technology.

[10] K. Thomsen and P. Sørensen. Fatigue loads for wind turbines operating in wakes. *Journal of Wind Engineering and Industrial Aerodynamics*, 80(1):121–136, March 1999.

[11] S. Macrí, S. Aubrun, A. Leroy, and N. Girard. Experimental investigation of wind turbine wake and load dynamics during yaw maneuvers. *Wind Energy Science*, 6(2):585–599, April 2021. Publisher: Copernicus GmbH.

[12] D. Mordasov. Numerical investigation of the wake-diffusion rotor concept. July 2022. MSc thesis. TU Delft.

[13] J. Schottler, J. Bartl, F. Mühle, L. Sætran, J. Peinke, and M. Hölling. Wind tunnel experiments on wind turbine wakes in yaw: redefining the wake width. *Wind Energy Science*, 3(1):257–273, May 2018.

[14] F. Mühle, J. Schottler, J. Bartl, R. Futrzynski, S. Evans, L. Bernini, P. Schito, M. Draper, A. Guggeri, E. Kleusberg, D. S. Henningson, M. Hölling, J. Peinke, M. S. Adaramola, and L. Sætran. Blind test comparison on the wake behind a yawed wind turbine. *Wind Energy Science*, 3(2):883–903, November 2018.

[15] I. Neunaber, M. Hölling, R. J. A. M. Stevens, G. Schepers, and J. Peinke. Distinct Turbulent Regions in the Wake of a Wind Turbine and Their Inflow-Dependent Locations: The Creation of a Wake Map. *Energies*, 13(20):5392, October 2020.

[16] P. Hulsman, M. Wosnik, V. Petrović, M. Hölling, and M. Kühn. Development of a Curled Wake of a Yawed Wind Turbine under Turbulent and Sheared Inflow. 2022. Wind Energy Science Vol. 7, 237-257, 2022.

[17] J. Bartl, I. Koi, M. Skoland, G. Stenfelt, and T. Hansen. Experiments on upstream induction and wake flow for multirotor wind turbines. *Journal of Physics: Conference Series*, 2505(1):012005, May 2023.

[18] S. Barber, Y. Wang, S. Jafari, N. Chokani, and R. S. Abhari. The Impact of Ice Formation on Wind Turbine Performance and Aerodynamics. *Journal of Solar Energy Engineering*, 133(011007), January 2011.

[19] C. Kress, N. Chokani, and R. S. Abhari. Passive minimization of load fluctuations on downwind turbines. *Renewable Energy*, 89:543–551, April 2016.

[20] G. Stenfelt and Western University of Applied Science. MarinLab. Retrieved from: https: www.hvl.no/contentassets/de9d0d0d3cc146f3a0782a81d34f8e13/marinlab_info.pdf Accessed on 25.04.2024.

[21] D. Lande-Sudall, S. Tolleifsen, K. Gravelsæter, H. Moen, and J. Bartl. Preliminary performance assessment from towing tank testing of a horizontal-axis turbine. *Proceedings of the European Wave and Tidal Energy Conference*, 15, September 2023.

[22] J Dang, J. Brouwer, R. Bosman, and C. Pouw. Quasi-Steady Two-Quadrant Open Water Tests for the Wageningen Propeller C- and D-Series. August 2012.

[23] I. M Viola, Alex Nila, Thomas Davey, and Roman Gabl. Underwater LED-based Lagrangian particle tracking velocimetry. *Journal of Visualization*, 25(5):1035–1046, October 2022.

[24] B. Wieneke. Improvements for volume self-calibration. *Measurement Science and Technology*, 29(8):084002, July 2018. Publisher: IOP Publishing.

[25] B. Weltzien, H. J. Jakobsen, and N. Arntzen. Design and construction of a turbine model for testing in MarinLab. May 2022. BSc thesis.

[26] A. Sciacchitano. Uncertainty quantification in particle image velocimetry. *Measurement Science and Technology*, 30, July 2019.

Appendix

Appendix A: Reference blade geometry

Reference blade geometry			
Section No.	Position [m]	Chord length [m]	Twist angle [°]
1	0.00	0.018	[-]
2	0.01	0.051	20.15
3	0.02	0.069	16.74
4	0.03	0.070	14.91
5	0.04	0.067	12.97
6	0.05	0.064	11.14
7	0.06	0.062	9.48
8	0.07	0.059	8.06
9	0.08	0.056	6.79
10	0.9	0.053	5.62
11	0.10	0.051	4.69
12	0.11	0.049	3.78
13	0.12	0.047	3.00
14	0.13	0.045	2.38
15	0.14	0.043	1.79
16	0.15	0.042	1.26
17	0.16	0.030	0.79
18	0.17	0.039	0.39
19	0.18	0.037	0.04
20	0.19	0.035	-0.29
21	0.20	0.033	-0.57
22	0.21	0.031	-0.82
23	0.22	0.028	-1.03
24	0.23	0.024	-1.34
25	0.24	0.018	-1.60
26	0.25	0.004	-1.79

Table 2: Blade geometry of the reference blade, inspired by ForWind [14]. First section is a circular airfoil and no twist angle is defined. Blade sections 2-26 are made of the SD7003-085-88 airfoil.

Appendix B: Twist angle and chord length distribution for all three rotor blades

	Ref. blade	35TA	45TA
Section No.	Twist angle [°]	Twist angle [°]	Twist angle [°]
1	[-]	[-]	[-]
2	20.15	35.00	45.00
3	16.74	27.98	35.22
4	14.91	22.36	27.57
5	12.97	17.87	21.58
6	11.14	14.29	16.89
7	9.48	11.42	13.22
8	8.06	9.13	10.35
9	6.79	7.30	8.10
10	5.62	5.83	6.34
11	4.69	4.66	4.96
12	3.78	3.73	3.89
13	3.00	2.98	3.04

Twist angle of all three rotor blades - Section 1-13

Table 3: Blade geometry for all three rotor blades. Only the modified sections are displayed. Section 14-26 have the same configuration as the corresponding sections in Table 2. Chord length and position are also the same. First section is a circular airfoil and no twist angle is defined.
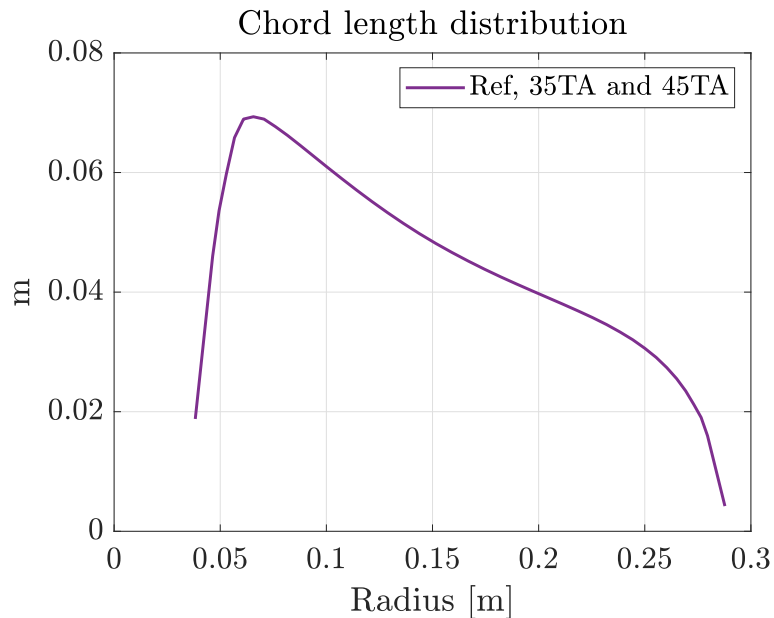

Figure 22: Chord length distribution. Same for all three blades.

Appendix C: Measurement procedures

C1: Torque and thrust measurement procedure

1. The turbine motor is turned on at target λ and let rotating for 2-3 seconds .

2. The recording of data from the torque sensor through the LabView software is started.

3. After recording data for approximately 10 seconds, the carriage is accelerated to its target towing speed and left running for 33 meters.

4. When the carriage decelerate at its endpoint, the recording of the data is left for another 5-10 seconds before the run is complete.

5. After the record button yet again is pressed to stop recording data, he turbine motor is shut off and the carriage is slowly pulled back to its starting position before a new run is conducted.

C2: LPTV-measurements procedure

1. Both carriages, with the turbine running at $\lambda = 6.0$ mounted on the front carriage and the PIV-system on the latter one, are accelerated to target speed 0.5 m/s.

2. When both carriages has been towed for 20 seconds, the image capturing is started.

3. Images are recorded for 15 seconds at 100 Hz, which results in 1500 images per run.

4. After 15 seconds of image recording, the carriages are stopped and the engine shut off.

5. Both carriages are slowly towed back to its starting position, and a new run is cinducted.

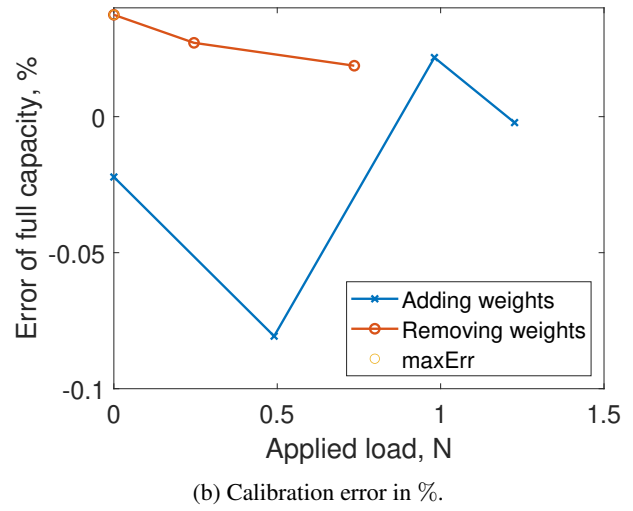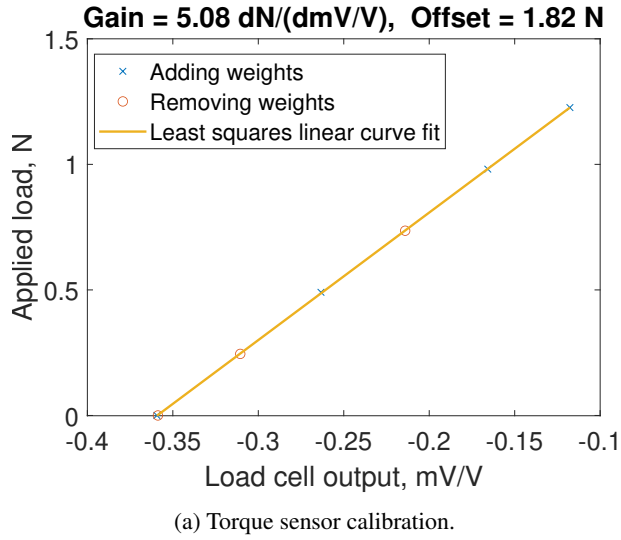# Appendix D: Calibration procedure

D1: Torque sensor calibration

(a) Torque sensor calibration.

(b) Calibration error in %.

Figure 23: Torque sensor calibration.

D2: Load cell calibration (thrust)

(a) Load cell calibration (thrust).
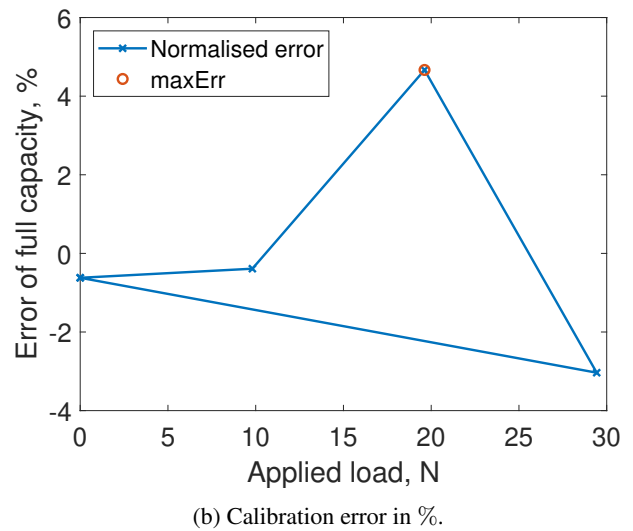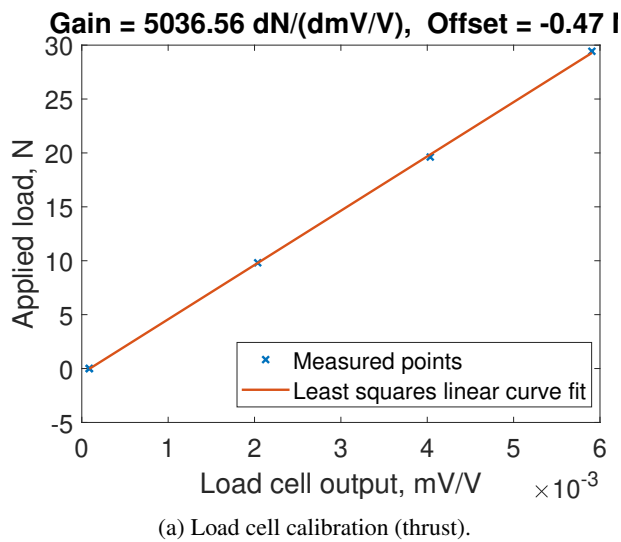
(b) Calibration error in %.

Figure 24: Load cell calibration.

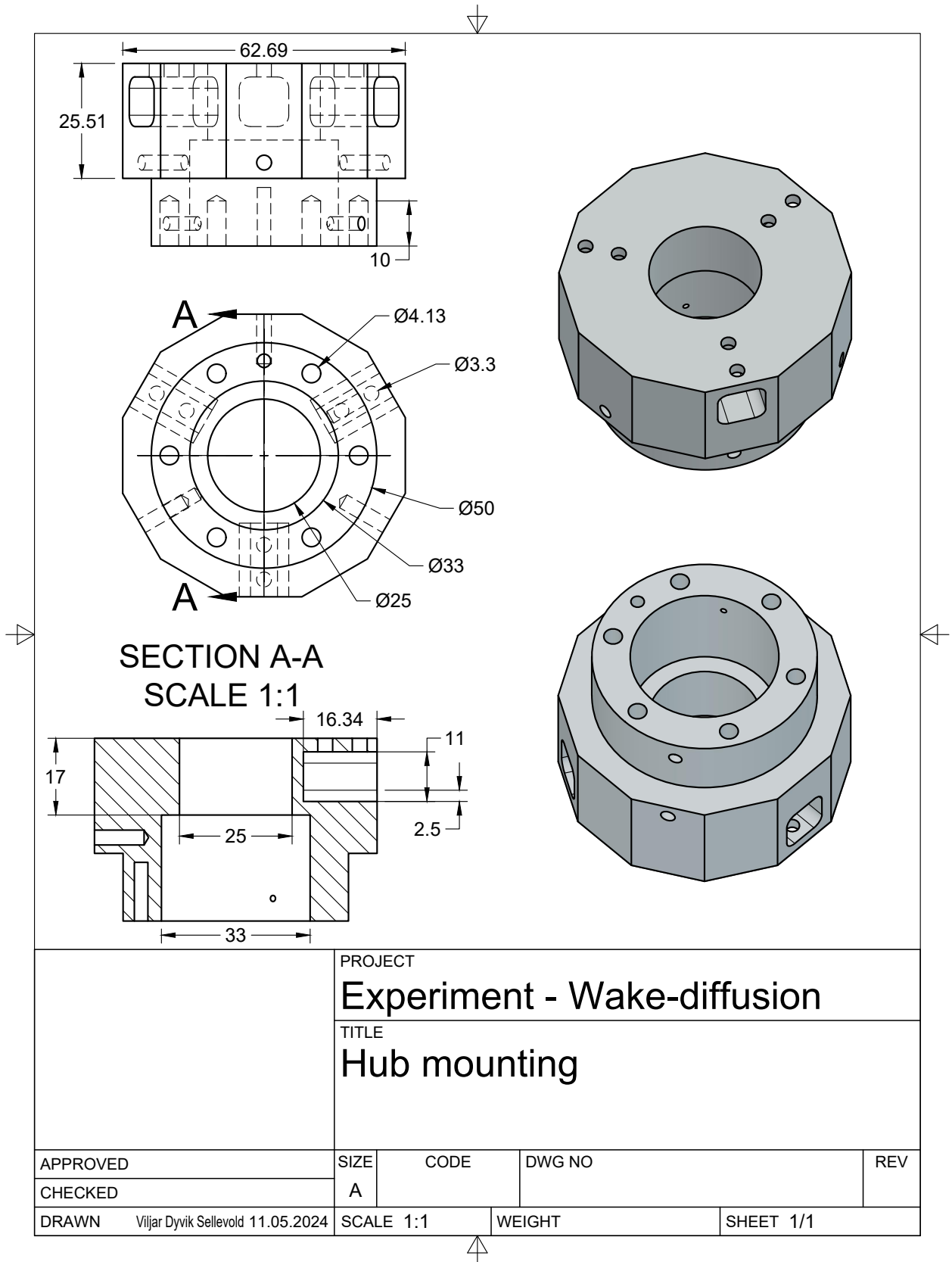## Appendix E: Drawings
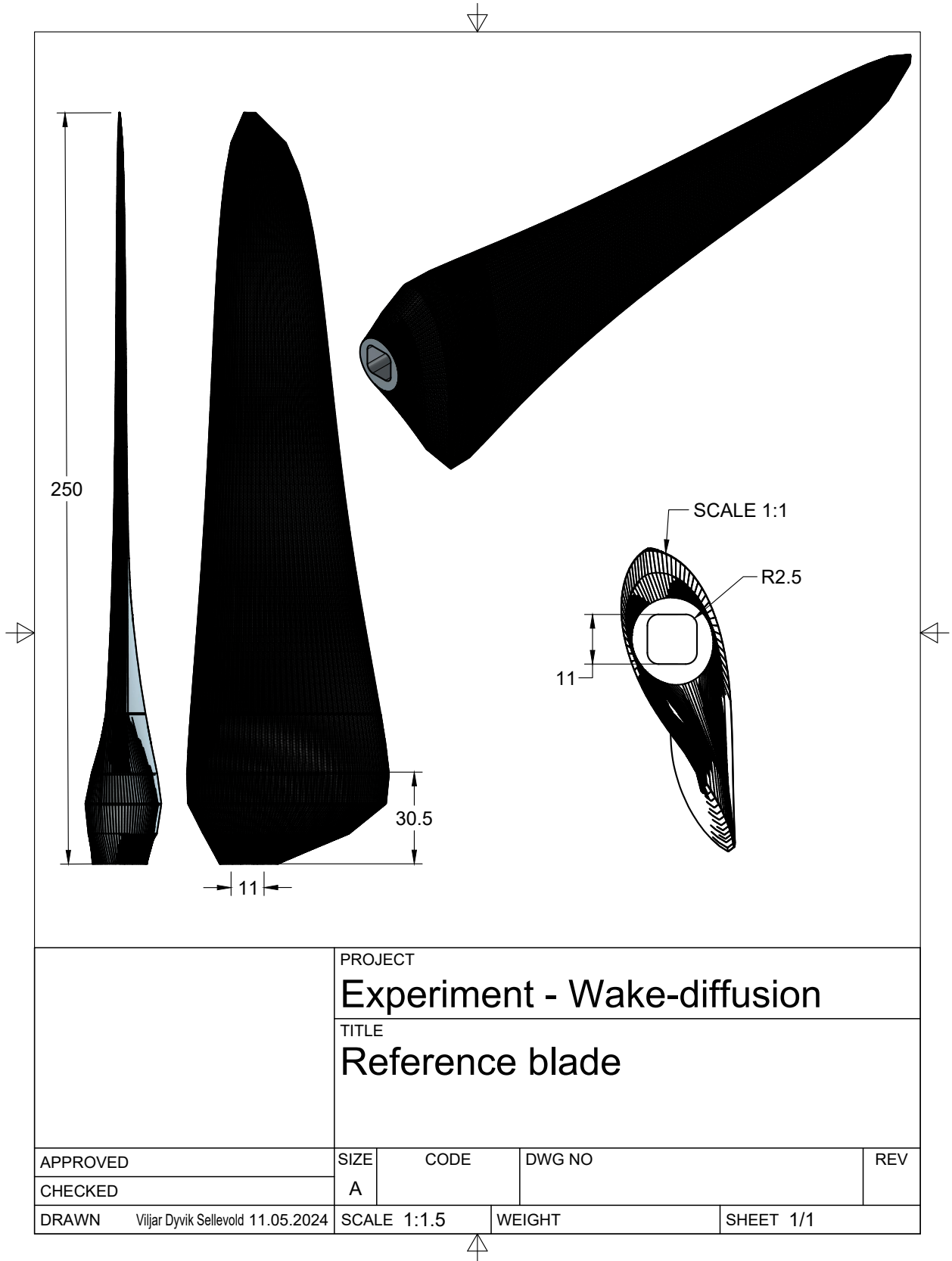
Figure 25: Reference blade.

62.69

25.51

10

A

A

Ø4.13

Ø3.3

Ø50

Ø33

Ø25

SECTION A-A
SCALE 1:1

16.34

11

17

25

2.5

33

	PROJECT			
	Experiment - Wake-diffusion			
	TITLE			
	Hub mounting			
APPROVED	SIZE	CODE	DWG NO	REV
CHECKED	A			
DRAWN Viljar Dyvik Sellevold 11.05.2024	SCALE 1:1	WEIGHT		SHEET 1/1

Figure 26: Hub mounting.

10

8.5

R35   R38
       R39
R25
14   1

78
Ø8.5
10   70   Ø5
102.75
50   10

PROJECT
Experiment - Wake-diffusion
TITLE
Sensor cover

APPROVED		SIZE	CODE	DWG NO		REV
CHECKED		A				
DRAWN	Viljar Dyvik Sellevold 11.05.2024	SCALE 1:2		WEIGHT	SHEET 1/1	

Figure 27: Sensor cover.

3.3   9   1.65   5

R35   R39   R38   R25

10   5   78

78   Ø5   70   102.75   72.75

PROJECT

Experiment - Wake-diffusion

TITLE

Sensor cover - Counter part

APPROVED		SIZE	CODE	DWG NO		REV
CHECKED		A				
DRAWN	Viljar Dyvik Sellevold 11.05.2024	SCALE 1:2	WEIGHT		SHEET 1/1	

Figure 28: Sensor cover - counter part.

Figure 29: Hub cover.

10.7

10.7

R2.5

54

17

R2.5

10.9

10.9

PROJECT				
Experiment - Wake-diffusion				
TITLE				
Connection piece between hub and blade				

APPROVED		SIZE	CODE	DWG NO		REV
CHECKED		A				
DRAWN	Viljar Dyvik Sellevold 11.05.2024	SCALE 1:1		WEIGHT	SHEET 1/1	
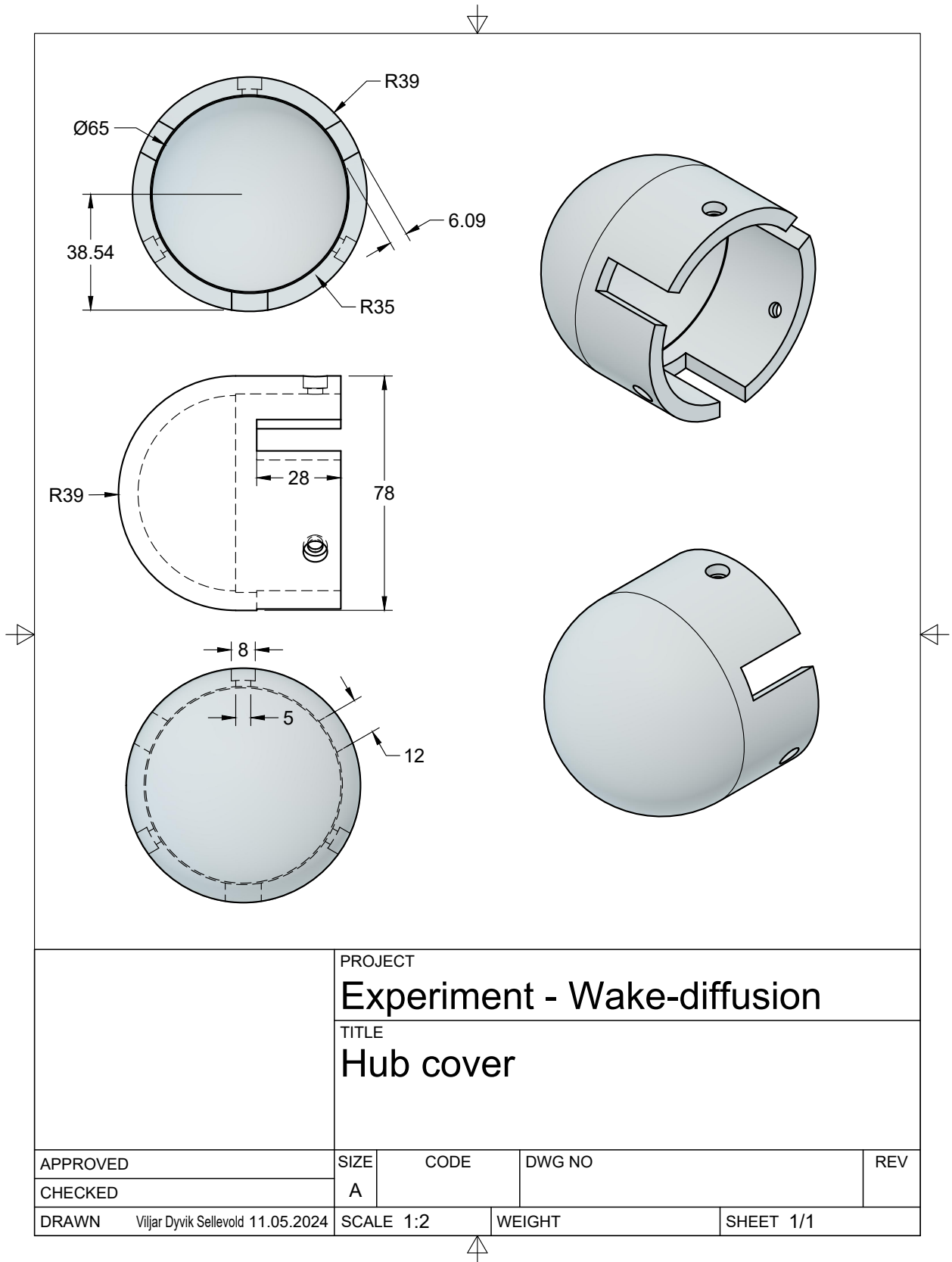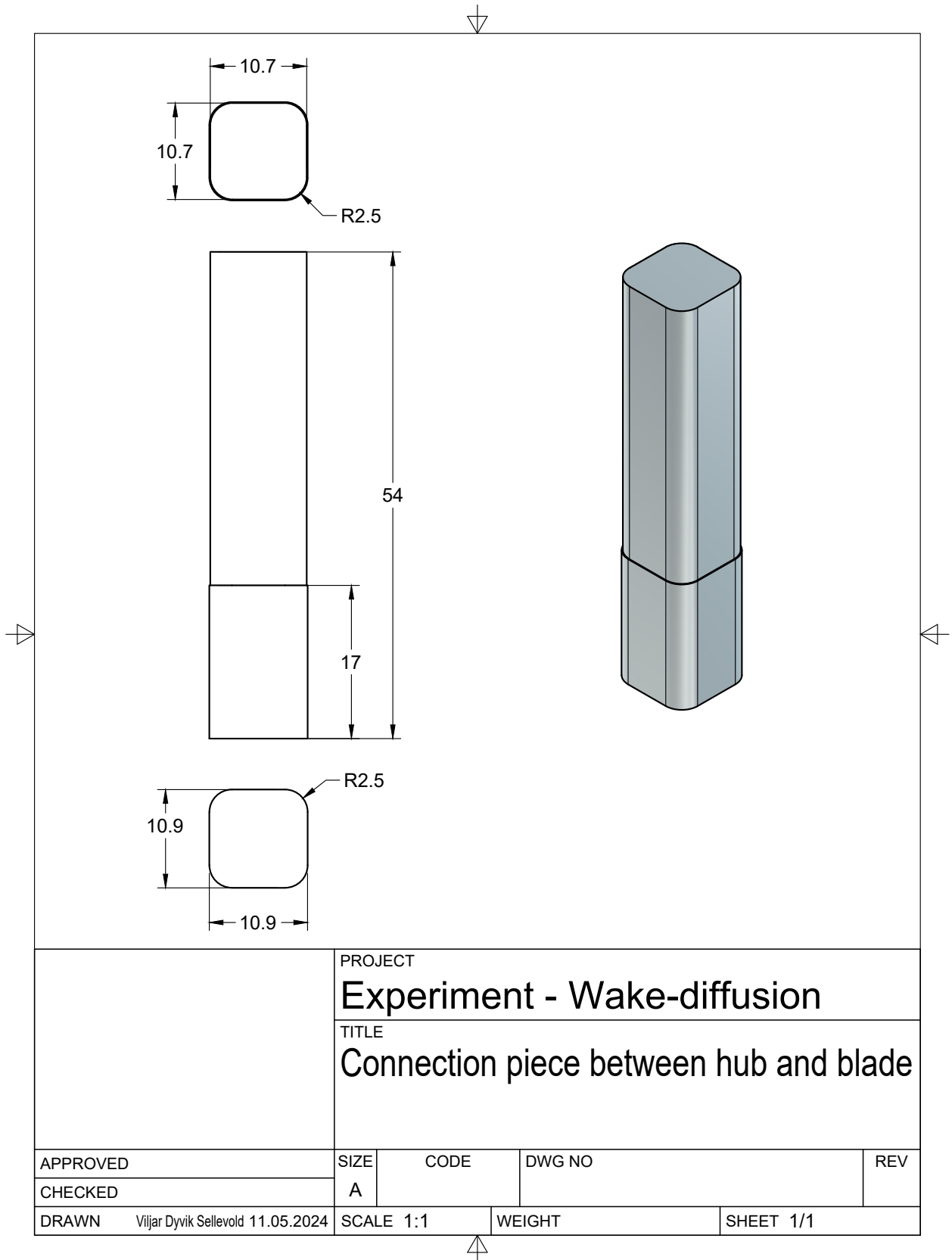
Figure 30: Connection piece between hub and rotor blade.

Appendix F: Measurement - Power and thrust coefficients

(a) C_P-values at u_0=0.4m/s.

(b) C_T-values at u_0=0.4m/s.
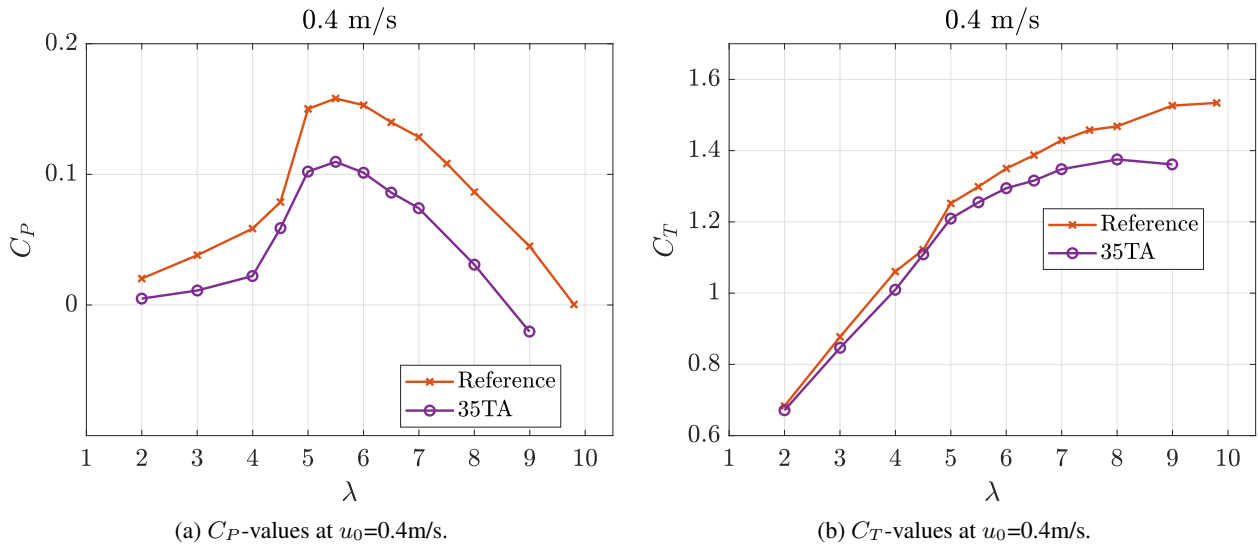
Figure 31: C_P and C_T-values at u_0=0.4m/s.

(a) C_P-values at u_0=0.6m/s.

(b) C_T-values at u_0=0.6m/s.
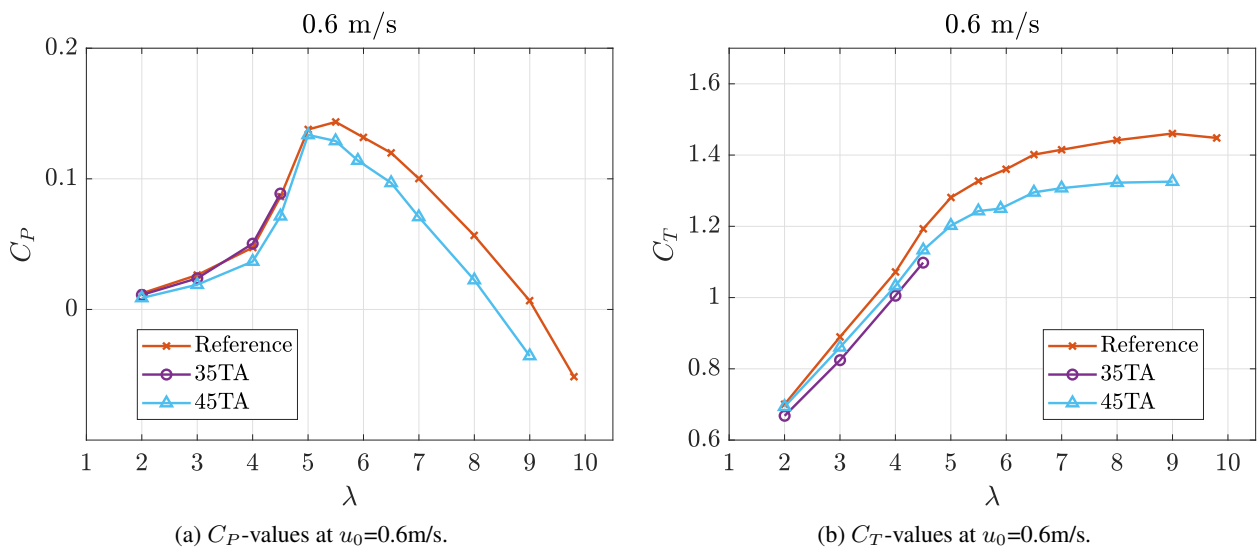
Figure 32: C_P and C_T-values at u_0=0.6m/s.

(a) C_P-values for 35TA
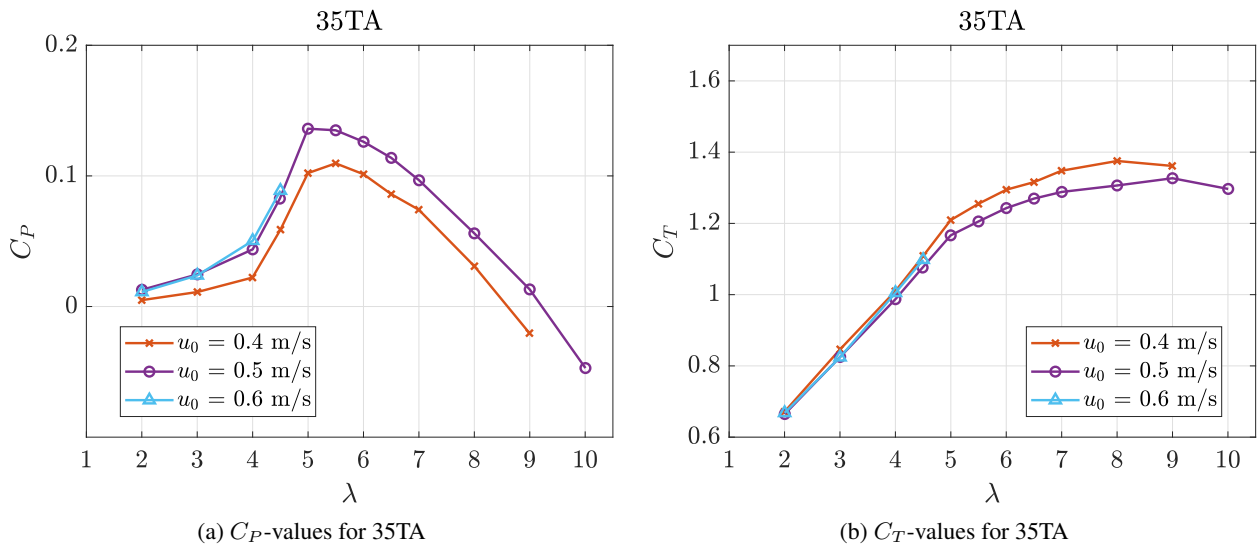
(b) C_T-values for 35TA

Figure 33: C_P and C_T-values for 35TA

(a) C_P-values for 45TA
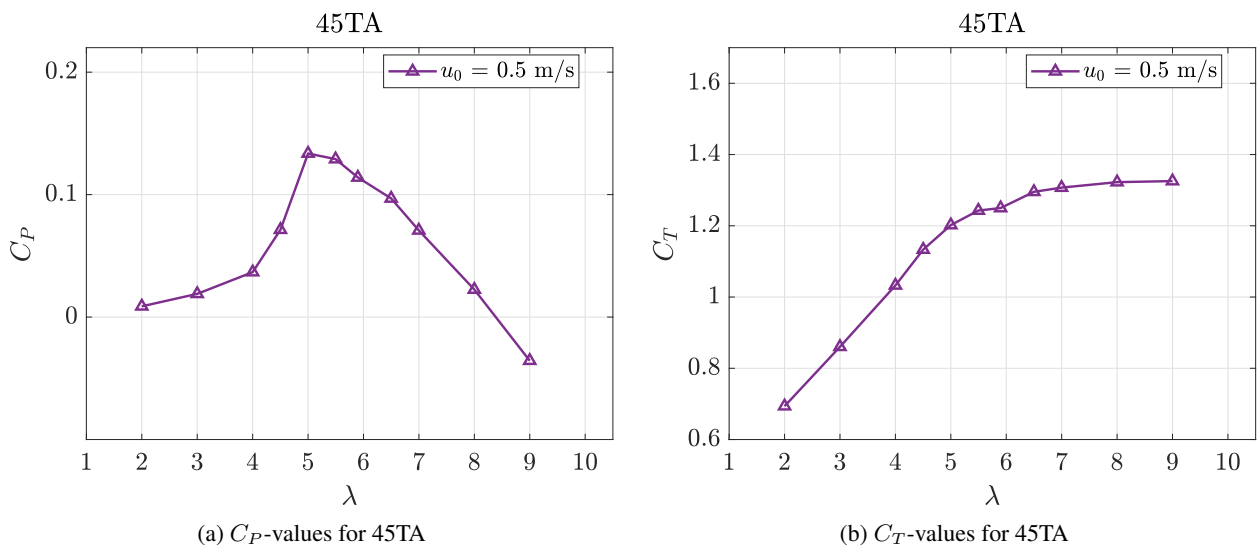
(b) C_T-values for 45TA

Figure 34: C_P and C_T-values for 45TA measured at u_0=0.5m/s.

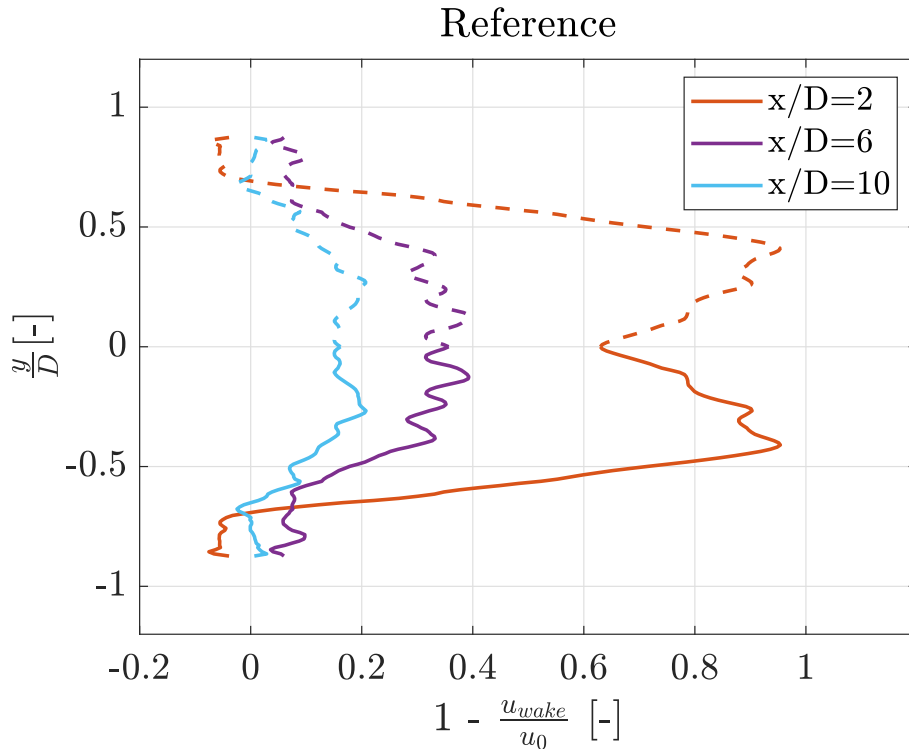**Appendix G: Measurement - Wake velocity profiles**

Reference

Figure 35: Wake velocity profiles for reference at different downstream distances.
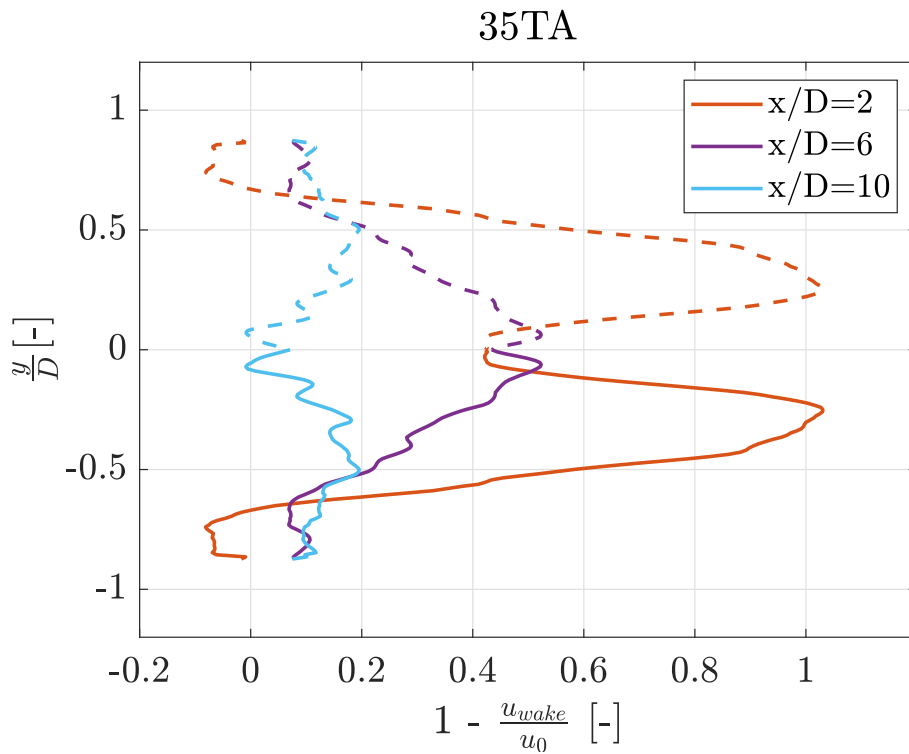
35TA

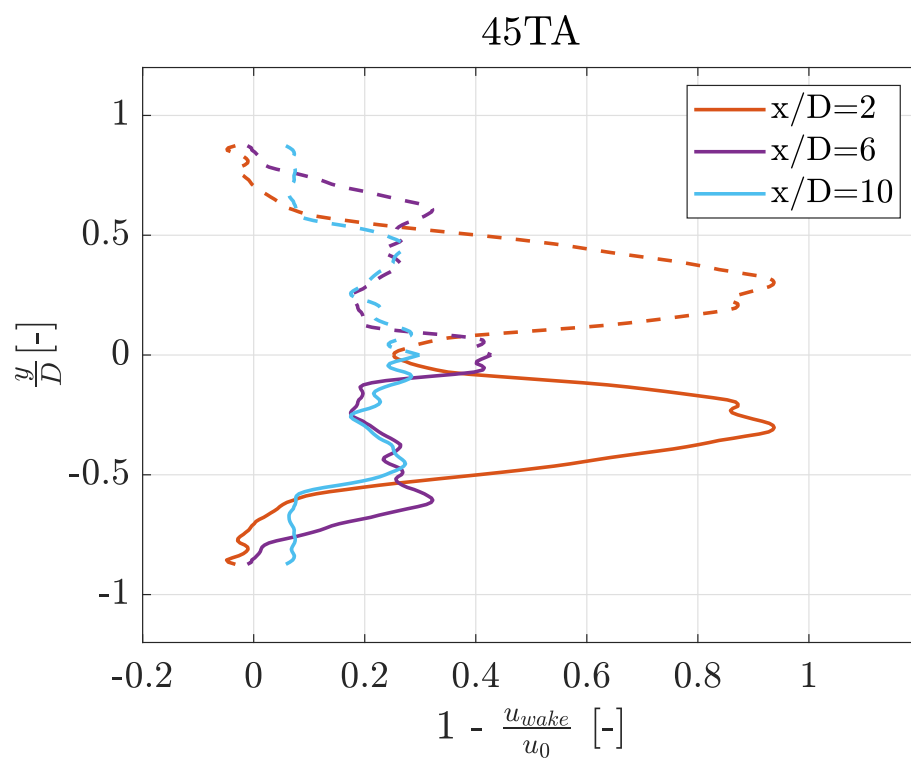Figure 36: Wake velocity profiles for 35TA at different downstream distances.

Figure 37: Wake velocity profiles for 45TA at different downstream distances.